Aus der Klinik für Radiologie

der Medizinischen Fakultät Charité – Universitätsmedizin Berlin

DISSERTATION

Time-resolved quantification of tissue structure by in vivo viscoelasticity measurements using magnetic resonance elastography

Zeitaufgelöste Charakterisierung von Gewebestrukturen mittels In-vivo-Bestimmung viskoelastischer Kenngrößen in der Magnetresonanz-Elastographie

zur Erlangung des akademischen Grades

Doctor of Philosophy (PhD)

vorgelegt der Medizinischen Fakultät

Charité – Universitätsmedizin Berlin

von

Felix Schrank

aus Magdeburg

Datum der Promotion: 26. Juni 2022

Table of contents

List of figures

repeated measurements. **B** Like ssMRE, gradient-echo spiral readout and low flip angle excitation, allows to acquire multiple images and sample multiple wave phases at a high frame rate. 16

List of tables

List of abbreviations

2D	Two-dimensional
3D	Three-dimensional
AA	Ascending thoracic aorta
AAb	Abdominal aorta
AD	Descending thoracic aorta
BMI	Body mass index
CAP	Cerebral arterial pulsation
CI	Confidence interval
EXT	Extensor digitorum longus
FDA	United States Food and Drug Administration
FFT	Fast Fourier transformation
FOV	Field of view
GAST	Gastrocnemius
ICC	Interclass correlation coefficient
***k*-MDEV**	Wavenumber-based multi-frequency dual elasto-visco inversion
LV	Left ventricle
MDEV	Multi-frequency dual elasto-visco inversion
MEG	Motion-encoding gradient
mn	Moment nulling
MR	Magnetic resonance
MRE	Magnetic resonance elastography
MRI	Magnetic resonance imaging
PER	Peroneus
PWV	Pulse wave velocity
RF	Radiofrequency
ROI	Region of interest
rtMRE	Real-time steady-state magnetic resonance elastography
SI	International System of Units
SNR	Signal to noise ratio

SOL	Soleus
ssMRE	Steady-state magnetic resonance elastography
SUV	Stroboscopic under-sampling of harmonic vibrations
SWS	Shear wave speed
TE	Time of echo
TIBA	Tibialis anterior
TIBP	Tibialis posterior
TR	Time of repetition

Abstract

Magnetic resonance elastography (MRE) is an emerging modality for quantitative viscoelasticity mapping of soft tissues in vivo. However, long acquisition times and poor temporal resolution limit the capacity of MRE to study moving organs and short-term temporal variations of viscoelasticity. Therefore, a new method for rapid time-resolved MRE has been developed based on a cardiac-gated steady-state MRE (ssMRE) pulse sequence with a multi-shot segmented spiral readout and respiratory navigation combined with stroboscopic displacement encoding and an adapted reconstruction algorithm. The method was extended to a single-shot real-time ssMRE (rtMRE) variant that can map non-periodic processes in a single measurement without any repeated readout.

The feasibility of the developed methods was demonstrated in 3 in vivo studies. In each study, time-resolved viscoelasticity maps on the order of $6-29$ Hz depicting stiffness (shear wave speed in m/s or magnitude of the complex shear modulus in Pa) and fluidity (phase of complex shear modulus in rad) were inverted and analyzed. In the first study, the influence of cerebral arterial pulsation (CAP) on the brain viscoelasticity was investigated in 12 healthy participants. In the second study, 20 healthy participants were examined to quantify differences in viscoelasticity along the aortic tree, including the ascending thoracic (AA), descending thoracic (AD), and abdominal (AAb) aorta. In a third study, rtMRE was applied to investigate dynamic muscle activation in the lower extremities during isometric plantar flexion and dorsiflexion in 15 healthy participants.

A global systolic CAP-induced decrease in stiffness of $6.6 \pm 1.9\%$ ($p < .001$) and a weak increase in fluidity of $0.5 \pm 0.5\%$ ($p = .002$) was found in the brain parenchyma. In the aorta, an increase in stiffness from the aortic root to the aortic bifurcation was found with 1.6 ± 0.2 m/s in AA, 2.4 ± 0.3 m/s in AD and 2.5 ± 0.6 m/s in AAb. In the muscle, it was observed that muscle activation is associated with significantly increased stiffness and fluidity. The most pronounced increase in viscoelastic parameters was observed in the soleus during plantar flexion (stiffness: $20.0 \pm 3.6\%$, fluidity: $41.3 \pm 12.0\%$, $p < .001$) and in the tibialis anterior during dorsiflexion (stiffness: $41.8 \pm 10.2\%$, fluidity: $27.9 \pm 2.8\%$, $p < .001$).

ssMRE and rtMRE proved to be versatile methods, yielding viscoelasticity maps with high spatial and temporal resolution. The results show CAP-induced transient effects on brain viscoelasticity, stiffness differences along the aortic tree, and an abrupt increase in stiffness and fluidity resulting from muscle activation. This dissertation contributes to the field of MRE by providing, for the first time, time-resolved viscoelasticity maps of soft tissues to study physiological processes in future diagnostic applications.

Zusammenfassung

Die Magnetresonanz-Elastographie (MRE) ist eine neue Methode zur quantitativen viskoelastischen Bildgebung von Weichgewebe in vivo. Allerdings sind die Möglichkeiten der MRE, bewegte Organe und kurzzeitige Variationen der Viskoelastizität zu untersuchen, aufgrund langer Messzeiten und geringer zeitlicher Auflösung begrenzt. Daher wurde eine schnelle zeitaufgelöste MRE-Methode auf Grundlage einer herzgetriggerten steady-state MRE-Pulssequenz (ssMRE) mit segmentierter Spiralauslese und Atemnavigation in Kombination mit stroboskopartiger Schwingungskodierung und angepasstem Rekonstruktionsalgorithmus entwickelt. Die Methode wurde zu einer Echtzeit-ssMRE-Variante (rtMRE) erweitert, die selbst nicht-periodische Prozesse in einer einzigen Messung ohne wiederholte Auslese abbilden kann.

Die Durchführbarkeit der Methoden wurde in 3 In-vivo-Studien überprüft. Dafür wurden zeitaufgelöste Viskoelastizitätskarten mit einer Bildrate von 6−29 Hz rekonstruiert, die die Steifigkeit (Scherwellengeschwindigkeit in m/s bzw. Magnitude des komplexen Schermoduls in Pa) und die Fluidität (Phase des komplexen Schermoduls in rad) der jeweiligen Gewebe abbilden. In der ersten Studie wurde der Einfluss der zerebral-arteriellen Pulsation (CAP) auf die Viskoelastizität des Gehirns von 12 gesunden Teilnehmern untersucht. In der zweiten Studie wurde bei 20 gesunden Teilnehmern die Viskoelastizität entlang des Aortenbaums, einschließlich der Aorta ascendens thorakal (AA), descendens thorakal (AD) und abdominales (AAb) quantifiziert. In der dritten Studie wurde mit der rtMRE dynamische Muskelaktivierung in den unteren Extremitäten während isometrischer Plantar- und Dorsalflexion bei 15 gesunden Teilnehmern analysiert.

Im Hirnparenchym wurde eine globale systolische Abnahme der Steifigkeit um $6{,}6 \pm 1{,}9\%$ ($p < .001$) und eine geringe Zunahme der Fluidität um $0{,}5 \pm 0{,}5\%$ ($p = .002$) festgestellt. Der Aortenbaum zeigte eine Zunahme der Steifigkeit von der Aortenwurzel bis zur Aortenbifurkation mit $1{,}6 \pm 0{,}2$ m/s in AA, $2{,}4 \pm 0{,}3$ m/s in AD und $2{,}5 \pm 0{,}6$ m/s in AAb. Ferner konnten bei Muskelaktivierung eine erhöhte Steifigkeit und Fluidität beobachtet werden. Den stärksten Anstieg wiesen der Soleus während der Plantarflexion (Steifigkeit: $20{,}0 \pm 3{,}6\%$, Fluidität: $41{,}3 \pm 12{,}0\%$, $p < .001$) und der Tibialis anterior während der Dorsalflexion (Steifigkeit: $41{,}8 \pm 10{,}2\%$, Fluidität: $27{,}9 \pm 2{,}8\%$, $p < .001$) auf.

ssMRE und rtMRE erwiesen sich als erfolgreiche Methoden für die Bildgebung von Viskoelastizität mit hoher räumlicher und zeitlicher Auflösung. Die Ergebnisse zeigen CAP-induzierte transiente Effekte auf die Viskoelastizität des Gehirns, Steifigkeitsunterschiede entlang des Aortenbaums und einen abrupten Anstieg der Steifigkeit und der Fluidität in Folge von Muskelaktivierung. Diese Dissertation leistet einen wichtigen Beitrag auf dem Gebiet der MRE, indem sie erstmalig zeitaufgelöste Viskoelastizitätskarten von Weichgewebe zur Untersuchung physiologischer Prozesse für zukünftige diagnostische Anwendungen bereitstellt.

1 Introduction

The importance of tissue mechanics

Biological soft tissue mechanics have been proven to play a crucial role in the progression of many diseases.[1] The intrinsic mechanical properties of tissue reflect the structural composition and are essential for tissue function.[2] Mechanical properties are physical properties that characterize the deformation behavior of materials as a result of the application of force. When deforming, biological soft tissue behaves viscoelastically, i.e., it exhibits the mechanical properties of an elastic solid and viscous fluid simultaneously.[1]

Many physiologic and pathological processes are characterized by alterations in the viscoelastic behavior of the tissue.[3] For example, liver fibrosis (i.e., the scarring of liver tissue in response to inflammation) is associated with increased stiffness when compared to healthy liver tissue.[4] The degree of liver stiffness is of significant clinical relevance because it is associated with an increased risk of decompensated cirrhosis, hepatocellular carcinoma, and death in patients with chronic liver disease.[5] Another example is carcinogenesis, which is generally associated with marked changes in tissue structure, reflected in a macroscopic change in the mechanical properties of the tumor lesion.[1] Overall, the elasticity and viscosity of a tumor mass reflect the mobility and metastatic potential of cancer cells.[1]

The viscoelastic properties of soft tissue are, therefore, highly sensitive biomarkers for diagnostic purposes. The comparison of different viscoelastic properties can help to separate healthy and non-healthy tissues and be used for the detection, characterization, and monitoring of disease and for assessing treatment outcome.

Magnetic resonance elastography

For centuries, manual palpation has been the tool of choice for physicians accessing the viscoelastic properties of soft tissues near the body surface. During palpation, the physician manually deforms the tissue and detects viscoelastic abnormalities through the sensation of touch. However, manual palpation has two major disadvantages: it is only feasible for easily accessible, superficial organs, and the findings are highly subjective.[1]

Elastography is an imaging-based approach to quantify the viscoelastic properties of tissues in vivo. The general principle of elastography is to excite a mechanical stress field in the tissue and then image the deformation of the tissue.[6] Based on the images of these deformations, mathematical algorithms can reconstruct the intrinsic viscoelastic properties. Various elastography techniques have been developed that differ in the type of force applied to the tissue, imaging modality selected, and parameter reconstruction used.[6] The two most common approaches are ultrasound elastography and magnetic resonance elastography (MRE).

MRE is a motion-sensitive phase-contrast magnetic resonance imaging (MRI) technique for imaging the viscoelastic properties of soft tissue. MRE uses externally induced time-harmonic vibrations in a low-frequency range, which penetrate deep into the target tissue and lead to local deformations on the order of a few tens of micrometers. A motion-sensitive pulse sequence is used to encode the induced oscillating

displacement fields into the complex magnetic resonance (MR) signal phase. Inversion algorithms are used to derive spatial maps of viscoelastic parameters from the displacement fields, depicting the stiffness or viscosity of soft tissues and organs pixelwise.

State-of-the-art MRE

Since the first clinical MRE paper, published in 1995[7], MRE has proven to be a useful diagnostic technique. Approved by the United States Food and Drug Administration (FDA) in 2009, a basic MRE device for the detection of liver fibrosis is commercially available for many types of MRI scanners. Research studies have applied MRE to the examination of a wide range of organs (such as the human brain, spleen, and female breast) and the detection of diseases (such as Alzheimer's disease, multiple sclerosis, and Parkinson disease).[1, 6]

While state-of-the-art MRE can reconstruct maps of spatially high-resolved viscoelastic parameters, it requires long image acquisition times (on the order of minutes) due to the MRE displacement encoding and repeated image acquisition. Long acquisition times and poor temporal resolution limit the ability of MRE to be used to study moving organs or to map the temporal variations in viscoelasticity for dynamic processes.[8] These limitations are particularly relevant when using MRE in muscle and the cardiovascular system, including the myocardium and the aortic tree.[8, 9] A fast MRE pulse sequence with rapid displacement encoding is needed to capture short-term temporally resolved alterations of viscoelastic parameters.

Objective of this work

This doctoral project aims to develop a versatile time-resolved MRE method that incorporates a new MRE pulse sequence, rapid displacement encoding, and post-processing adapted for time-resolved viscoelastic parameter reconstruction. To this end, a cardiac-gated steady-state MRE (ssMRE) pulse sequence with multi-shot segmented spiral k-space readout has been developed and combined with continuous stroboscopic displacement encoding. The developed method was further extended towards a single-shot ssMRE with interleaved stroboscopic displacement encoding to allow for the measurement of viscoelasticity in real-time. Both approaches, ssMRE and real-time ssMRE (rtMRE), described herein provide, for the first time, viscoelastic parameters in high time resolution for imaging moving organs and physiological processes. Three pilot studies will demonstrate the feasibility and performance of the method for the brain, aorta, and skeletal muscle in healthy participants:

- **Study 1:** Cardiac-gated steady-state multifrequency magnetic resonance elastography of the brain: Effect of cerebral arterial pulsation on brain viscoelasticity[10]

- **Study 2:** Steady-state multifrequency magnetic resonance elastography of the thoracic and abdominal human aorta—validation and reference values[11]

- **Study 3:** Real-time MR elastography for viscoelasticity quantification in skeletal muscle during dynamic exercises[12]

Motivation of the presented studies

The first application of ssMRE, Study 1 [10], investigates how cerebral arterial pulsation (CAP) affects brain viscoelasticity during the cardiac cycle. CAP relies on cerebral vascular compliance, an adaptive change in blood volume in response to changing blood pressure.[13] Many neurological disorders are related to the impaired vascular function of the brain, eventually leading to chronically hypoxic regions, dysregulated metabolic activity, or cerebral amyloid deposition.[14, 15] However, there is still a lack of viable biomarkers that can directly quantify cerebral vascular compliance in vivo.[13] While MRE is potentially sensitive to vascular compliance,[16] classical MRE techniques eliminate the appearance of any time-dependent influence of CAP on brain viscoelasticity due to the long image acquisition time over multiple cardiac cycles.[10] The developed cardiac-gated ssMRE method provides 99 images of viscoelastic parameters with a 25-Hz frame rate covering 4 s encompassing multiple cardiac cycles and allowing for the time-dependent influence of CAP on brain viscoelasticity to be captured.[10] Time courses of stiffness, fluidity, and CAP-signal were analyzed for effect size, timing, and age effects. The findings serve as the first reference values for viscoelasticity variation in the healthy brain over the cardiac cycle.[10]

We then applied the cardiac-gated ssMRE approach to the cardiovascular system and studied the human aortic tree. The purpose of Study 2 [11] is to test the feasibility of using ssMRE to quantify viscoelastic parameters of the thoracic and abdominal aorta in vivo. Aortic stiffness is an important and independent risk factor for hypertension and cardiovascular disease.[17, 18] In clinical practice, the measurement of carotid-femoral pulse wave velocity (PWV) is the gold standard for determining aortic stiffness.[19] However, it is known that PWV measurements are prone to error due to assumptions of an excessively simple geometry of the aorta.[19] Although aortic MRE has excellent potential, it remains a challenge due to rapid movement caused by the cardiac cycle and breathing, and only sparse abdominal data have been reported.[9] The developed ssMRE approach allows for full displacement encoding within a diastolic time window. Viscoelastic properties were derived from 32 images at a frame rate of 28.6 Hz throughout the cardiac cycle.[11] ssMRE derived viscoelasticity maps were then analyzed in three aortic segments along the aortic tree: ascending thoracic (AA), descending thoracic (AD), and abdominal (AAb) aorta.[11] The study reports the first reference values of diastolic stiffness and fluidity of the AA and AD in healthy participants of different ages.[11]

Finally, in Study 3 [12], we applied rtMRE to map dynamic muscle activities in real-time. In general, elastography is well-suited to quantify muscle activity in a clinical setting, for example, in rehabilitation and sports medicine.[8] To date, MRE is limited to study the viscoelastic parameters of muscles in a constant static state or when assuming periodic changes where MRE imaging can be repeatedly synchronized.[12] The possibility of real-time viscoelasticity imaging is, in particular, relevant for muscles that undergo non-periodic activities, like skeleton muscles or cardiac muscles during arrhythmia. rtMRE provides viscoelasticity maps covering 30.6 s at a frame rate of 5.9 Hz, which is considered to be a real-time representation of the loading cycle of the skeletal muscles, which occurs on the order of seconds.[12] The developed approach was demonstrated in the lower extremity muscles of healthy participants who voluntarily performed isometric plantar flexion and dorsiflexion exercises. Six muscles were analyzed for

changes in viscoelastic parameters induced upon the exercises. Of these muscles, the gastrocnemius (GAST), soleus (SOL), peroneus (PER), and tibialis posterior (TIBP) belong to the posterior compartment of the lower leg, acting as a plantar flexors.[12] The tibialis anterior (TIBA) and extensor digitorum longus (EXT) belong to the anterior compartment, acting as dorsiflexors.[12] This study reports, for the first time, on imaging dynamic and non-periodic processes and demonstrates an instantaneous viscoelastic response to muscle activity measured by MRE.[12]

2 Background

2.1 Viscoelasticity theory

The complex shear modulus

The relationship between stress and strain describes the deformation response of materials as a consequence of an applied force.[20] Materials that exhibit elastic behavior will deform immediately when a stress is applied. Elastic deformations will be completely restored when the force is removed. In the case of small elastic deformations, we can formulate a linear relationship of stress and strain using Hooke's law written as

$$\sigma_{ij} = C_{ijkl}\epsilon_{kl} \tag{2.1}$$

where σ_{ij} is the stress tensor, ϵ_{kl} is the strain tensor, and C_{ijkl} is a fourth-ranked elasticity tensor with 81 elements quantifying the resistance of the material to deformation.[1] Because of the symmetrical properties of the strain and stress tensors and the scalar strain energy, the number of independent elements of the elasticity tensor can be reduced to 21.[21] To further reduce the number of independent coefficients, we assume isotropy. An isotropic elastic material can be characterized with only two independent parameters as follows,

$$\sigma_{ij} = \lambda\theta\delta_{ij} + 2\mu\epsilon_{ij} \tag{2.2}$$

where λ and μ are known as the Lamé parameters, θ is the cubic dilation, and δ_{ij} is the Kronecker delta. We further assume that soft tissue is incompressible ($\theta = 0$, $\lambda \to \infty$).[1] It is, therefore, possible to express the relationship of equation (2.2) for a linearly elastic, isotropic, and incompressible material using only the second Lamé parameter by

$$\sigma_{ij} = 2\mu\epsilon_{ij} \tag{2.3}$$

where the second Lamé parameter, μ, is identical to the shear modulus.[21] A high shear modulus implies a high resistance to shear deformation, i.e., high stresses are required to shear the material; it is a stiff material.

Viscous materials accumulate deformation time-dependently at a given rate when stress is applied.[1] Like honey, viscous materials "flow" into the new distorted form. Viscous deformation is irreversible, i.e., the material retains the distorted shape even after the force is removed. To account for the rate of deformation, we consider here the strain rate. Similar to Hooke's law for incompressible isotropic viscous fluids and small (laminar) stress fields, we can formulate the stress proportional to the strain rate given by

$$\sigma_{ij} = 2\eta\dot{\epsilon}_{ij} \tag{2.4}$$

where η is the viscosity and $\dot{\epsilon}$ is the strain rate.[21] Since MRE utilizes time-harmonic oscillating stress fields, we use the formula of the strain-rate $\dot{\epsilon}_{ij} = i\omega\epsilon_{ij}$ and formulate

$$\sigma_{ij} = 2\eta\mathrm{i}\omega\epsilon_{ij} \tag{2.5}$$

where ω is the angular frequency.[22] From equation (2.5), we can see that in the viscous case there is a frequency dependence due to the term ω.

Biological soft tissues behave viscoelastically when force is applied, i.e., they exhibit the properties of elastic and viscous materials at the same time.[1] To formulate the stress and strain relationship in the case of viscoelasticity, we have to combine equations (2.3) and (2.5). In this context, we introduce the complex shear modulus, which represents the second Lamé parameter for viscoelastic materials in the case of a time-harmonic stress field, written as

$$\sigma_{ij} = G^* 2\epsilon_{ij} \tag{2.6}$$

where G^* is the complex shear modulus defined by

$$G^* = G' + \mathrm{i}G'' = \mu + \mathrm{i}\omega\eta \tag{2.7}$$

where the real part G' is the storage modulus, and the imaginary part G'' is the loss modulus, characterizing the elastic and viscous behaviors, respectively.[1] Henceforth, we will represent G^* in terms of its magnitude $|G^*|$ and phase angle φ, written as

$$G^* = |G^*| \cdot e^{\mathrm{i}\varphi} \tag{2.8}$$

where φ (also called loss angle) is defined as the ratio of the loss modulus to the storage modulus by

$$\tan(\varphi) = \frac{G''}{G'} \tag{2.9}$$

The complex shear modulus is represented between two limits, pure solid and pure fluid behaviors. In the case of an ideal elastic material, G^* becomes real-valued with $G^* = G' = \mu$ and φ equals zero. In the case of purely viscous materials, G^* becomes $G^* = G'' = \mathrm{i}\omega\eta$, and φ comes close to $\pi/2$. Typically, biological soft tissue is viscoelastic and exhibits G' and G'' greater than zero and φ values within the limits of zero (elastic) to $\pi/2$ (viscous). Furthermore, G^* is frequency-dependent due to the loss modulus $G'' = \mathrm{i}\omega\eta$. Henceforth, we will use $|G^*|$ as the parameter for tissue stiffness and the phase angle φ as a surrogate of fluidity. The SI units of $|G^*|$ and φ are pascal and radian, respectively.

Time-harmonic mechanical waves in a viscoelastic soft tissue

We now formulate the relationship between the derived G^* and a measured displacement field due to time-harmonic mechanical waves. Mechanical waves in an infinite, homogeneous, isotropic, viscoelastic, and incompressible material can be described by the Helmholtz equation, which is written

$$\rho \frac{\partial^2 \boldsymbol{u}}{\partial t^2} = G^* \nabla^2 \boldsymbol{u} \tag{2.10}$$

where ρ is the material's density, $\boldsymbol{u}$ is the vector displacement field, and t is time.[1] The term $G^*\nabla^2\boldsymbol{u}$ in equation (2.10) describes purely shear strain and represents the transversely polarized shear wave field.

Equation (2.10) has the form of the general wave equation[1], so, we can obtain the shear wave speed SWS by

$$SWS = \frac{1}{\mathrm{Re}\left(\sqrt{\frac{\rho}{G^*}}\right)} = \sqrt{\frac{2|G^*|}{\rho \cdot (1 + \cos(\varphi))}} \tag{2.11}$$

From equation (2.11) we can see that SWS is directly linked to the G^* of the material. Thus, SWS has similar frequency-dependent characteristics to G^*, due to the imaginary part $G'' = i\omega\eta$. Given the definition of

$$SWS = \Lambda \cdot f \tag{2.12}$$

where Λ is the wavelength and f is the frequency, we can see that SWS also mirrors the wavelength.

Overall, stiff tissue exhibits high $|G^*|$, high SWS, and long wavelengths, while less stiff tissue exhibits low $|G^*|$, low SWS, and short wavelengths. In addition to $|G^*|$, we will hereinafter also use SWS as a surrogate for tissue stiffness. The SI unit of SWS is meters per second.

2.2 MRE

MRE uses motion-sensitive MR gradients to image externally induced time-harmonic mechanical waves (vibrations) in soft tissue. Based on the characteristics of the imaged displacement field, more precisely, the wavelength and dispersion of the induced shear waves, inversion algorithms can reconstruct the intrinsic viscoelastic properties of the tissue. The main principles of MRE can be divided into three parts: vibration excitation, displacement encoding, and inversion of viscoelastic parameters.

Excitation of vibrations

Various external actuator systems have been developed to excite time-harmonic mechanical vibrations in tissue in clinical practice. Due to its simplicity and wide availability in a clinical environment, pneumatic actuator systems, such as those that use air pads (see Figure 1), are becoming increasingly popular. The majority of clinical MRE applications use vibrations in the low-frequency range from $20-100$ Hz.[1] The size and structure of the target tissue must be taken into account when selecting a vibration frequency, as the wavelength of the shear wave is frequency-dependent. High frequencies result in small wavelengths and attenuate quickly, while low frequencies have long wavelengths and can penetrate deeper organs. The vibration frequency in MRE is therefore study- and organ-dependent. Multifrequency MRE captures displacement fields of different frequencies to avoid low signal to noise ratio (SNR) due to standing wave nodes and inhomogeneous penetration due to attenuation effects.[1]
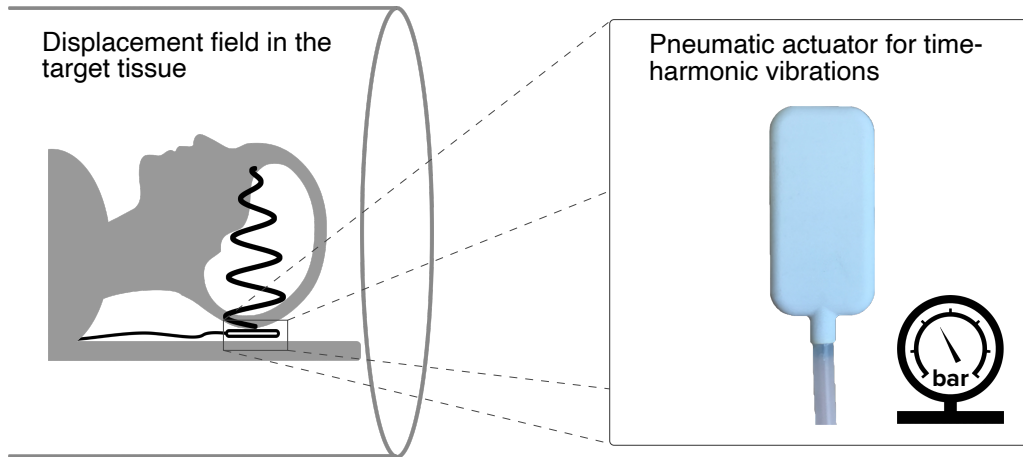
Figure 1. Illustration of vibration excitation using a brain MRE in a clinical setup as an example. Pneumatic actuators are positioned at the back of the participant's head within the MRI unit. During measurement, the actuators induce sinusoidal harmonic vibrations in the low-frequency range, which penetrate the brain tissue and cause local displacement fields on the order of micrometers. These displacement fields can be encoded in the phase of the complex MR signal to enable the inversion of intrinsic viscoelastic parameters.

Displacement encoding

MRE employs balanced motion-encoding gradients (MEG) to encode oscillating, time-harmonic tissue displacement into the phase of the complex MR signal. Different MEG waveforms are used to encode oscillating spins, while stationary spins or laminar spins at constant velocity are suppressed. With a balanced sinusoidal 0th order MEG moment nulling (mn), all moving spins accumulate a net phase signal, while stationary spins do not accumulate any signal.[1] A balanced, cosine-shaped 0th and 1st order mn, additionally eliminates any net phase signal from spins moving at a constant velocity, such as those seen with laminar flow.[1] Both orders of MEG have different sensitivity levels.[1] The selection of the MEG waveform and motion encoding period is always a compromise between signal loss and encoding efficiency. In order to capture complete tissue displacement, MRE image acquisition with motion encoding using MEGs is typically repeated on all three gradient axes: slice-select, phase-encoding, and readout.

The phase of the acquired MR signal is mapped on -π to π. If the accumulated phase signal exceeds beyond these limits, we have to adjust for phase wraps. In this case, the acquired phase values that exceed the range are mapped to the opposite end of the range, yielding so-called phase wraps. MRE, therefore, usually requires phase unwrapping algorithms to restore the correct phase values.

The MRE signal phase is a superposition of static magnetic field inhomogeneities, susceptibility effects, and time-harmonic-induced displacement fields.[1] To extract only the time-harmonic phase modulations, we have to acquire multiple images of different phases of a wave cycle at equidistant time steps. A temporal fast Fourier transformation (FFT) thereafter extracts the induced and encoded fundamental frequencies and yields complex-valued wave images. In practice, image acquisition is initiated with a certain time delay between each image, usually eight in total, to capture different time steps of the wave cycle (see Figure 2). This approach requires synchrony between the induced vibration and image acquisition to capture the wave

cycle at well-defined sample points. The complex-valued displacement field (derived after unwrapping and temporal FFT) is still a superposition of shear waves and compression waves. The effect of the compression waves can be removed by applying the curl operator to the complex-valued displacement field.[6] State-of-the-art multi-frequency MRE requires repeated measurements of three MEGs on orthogonal gradient axes, eight time steps, and several frequencies to reconstruct an elastogram.
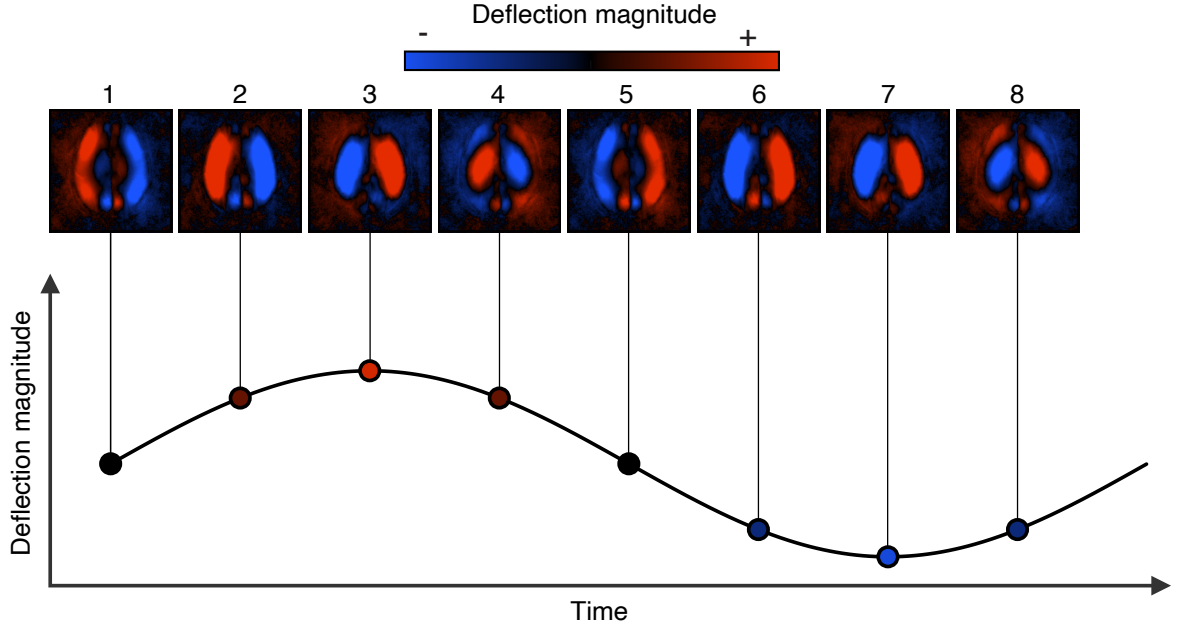
Figure 2. Wave cycle over time. To separate the induced time-harmonic modulations from the static phase modulations, MRE requires the imaging of the different phases of the wave cycle. In practice, image acquisition is typically repeated eight times with an individual time delay to capture eight equidistant time steps. The images above show a transverse view of 2-dimensional displacement fields in the human brain over time. The phase of the induced displacement field is color coded for high (red) and low (blue) levels of displacement. The induced sinusoidal waves propagated from the skull bone to the lateral ventricles.

Viscoelastic parameter reconstruction

Various MRE inversion algorithms have been published so far to reconstruct viscoelastic parameters, such as $|G^*|$, SWS, and φ, from complex-valued wave images. The two most widely used inversion algorithms for multi-frequency MRE are: multi-frequency dual elasto-visco inversion (MDEV) and wavenumber-based MDEV (*k*-MDEV).

The MDEV algorithm is a direct inversion approach that solves the Helmholtz equation, equation (2.10), and independently reconstructs the magnitude and phase angle of G^* by

$$|G^*| = \rho \frac{\sum_{i=1}^{N} \sum_{j=1}^{M} \omega_i^2 \left| \tilde{u}_j(\omega_i) \right|}{\sum_{i=1}^{N} \sum_{j=1}^{M} \left| \Delta \tilde{u}_j(\omega_i) \right|} \tag{2.13}$$

$$\varphi = \arg\left(\sum_{i=1}^{N} \sum_{j=1}^{M} \tilde{u}_j(\omega_i) \cdot \Delta \tilde{u}_j^{\dagger}(\omega_i) \right) \tag{2.14}$$

with N frequencies, M MEG components, wave image $\tilde{u}_j$, and † denoting complex conjugation.[23, 24] However, the frequency averaging in equations (2.13) and (2.14) ignores the fact that soft tissue has a frequency dependence and assumes a purely elastic material to simplify the calculations.[1] A major disadvantage of the MDEV inversion is the second-order derivative operator. Derivatives are noise-enhancing and give rise to a biased frequency dispersion of viscoelastic parameters.[1] Nevertheless, the MDEV algorithm is particularly widespread in brain MRE and reconstructs elastograms that are rich in detail.

k-MDEV, also known as tomoelastography, is a phase gradient approach that relies on first-order wave number reconstruction and amplitude-weighted averaging before inversion.[25] Tomoelastography uses directional filters, which decompose the complex-valued wave image $\tilde{u}_j$ into plane waves propagating in n different directions given by ϑ_n. Unlike MDEV, the tomoelastography inversion reconstructs SWS and reads

$$\frac{1}{SWS(\boldsymbol{r})} = \frac{\sum_{i,j,n} \frac{k'_{(j)}(\boldsymbol{r}, \omega_i, \vartheta_n)}{\omega_i}}{\sum_{i,j,n} W_{i,j,n}} \tag{2.15}$$

with frequencies i, MEG components j, at given point $\boldsymbol{r}$, with $\mathrm{k}'_{(j)}$, the real part of the complex wave vector given by

$$k'_{(j)} = \left\| \nabla^{(2D)} \left(\frac{\tilde{u}_j}{|\tilde{u}_j|} \right) \right\| \tag{2.16}$$

and an empirical weighting factor defined as $W_{i,j,n} = |u_j(r, \omega_i, \vartheta_n)|^4$.[25] Tomoelastography uses first-order derivatives and is, therefore, more noise-robust and widely used in clinical MRE of the abdomen.[1]

3 Methods

3.1 Subjects

All three studies[10-12] were approved by the ethics committee of the Charité – Universitätsmedizin Berlin in accordance with the World Medical Association Declaration of Helsinki (Ethical Principles for Medical Research Involving Human Subjects). Healthy participants of at least 18 years of age were investigated, excluding those with study-related abnormalities and risk factors. Each participant gave written informed consent to participate. Physiological parameters such as age, sex, height, and weight were documented, and the body mass index (BMI) was calculated.

In studies 1[10] and 2[11], the blood pressure and heart rate were recorded for each participant while resting in a seated position. In Study 2[11], PWV was measured before the MRE examination using an arm cuff-based oscillometer device (Agedio B900/Mobil-o-graph, I.E.M. GmbH, Stolberg, Germany).

Table 1. Physiological parameters of the participants (data given in mean ± standard deviation).[10-12]

	Study 1[10]	Study 2[11]	Study 3[12]
Number of participants	12 (0 female)	20 (3 female)	15 (2 female)
Age (years)	36 ± 11	40 ± 17	35 ± 10
Age range (years)	23 − 58	24 − 77	24 − 58
Weight (kg)	83 ± 9	79 ± 13	80 ± 14
Body mass index (BMI; kg/m^2)	24 ± 3	24 ± 3	24 ± 3
Systolic blood pressure (mmHg)	123 ± 9	123 ± 9	
Diastolic blood pressure (mmHg)	73 ± 10	79 ± 8	
Pulse wave velocity (PWV; m/s)		6.5 ± 2.1	

3.2 MRE experimental setup

All MRE experiments were performed on a clinical 1.5 Tesla MRI unit (Siemens, Magnetom Sonata, Erlangen, Germany).[10-12] Continuous harmonic vibrations were induced by a pneumatic air driver, comprised of a compressed air hose and 3D-printed, flat, bottle-shaped actuators. The actuators were positioned close to the target tissue (see Figure 3).

In Study 1[10], two actuators were placed in a birdcage single-element head coil directly underneath the head of the participant in supine position (see Figure 3A). In order to induce predominantly left-to-right head motion, the actuators were switched to an opposed-phase mode.[10] In three consecutive experiments, vibrations frequencies of 20 Hz, 31.25 Hz and 40 Hz were induced. Imaging was performed in a transverse slice through the center of the cerebrum, parallel to a line from the genu to the rostrum of the corpus callosum.[10] A fingertip pulse oximeter was used for cardiac triggering.
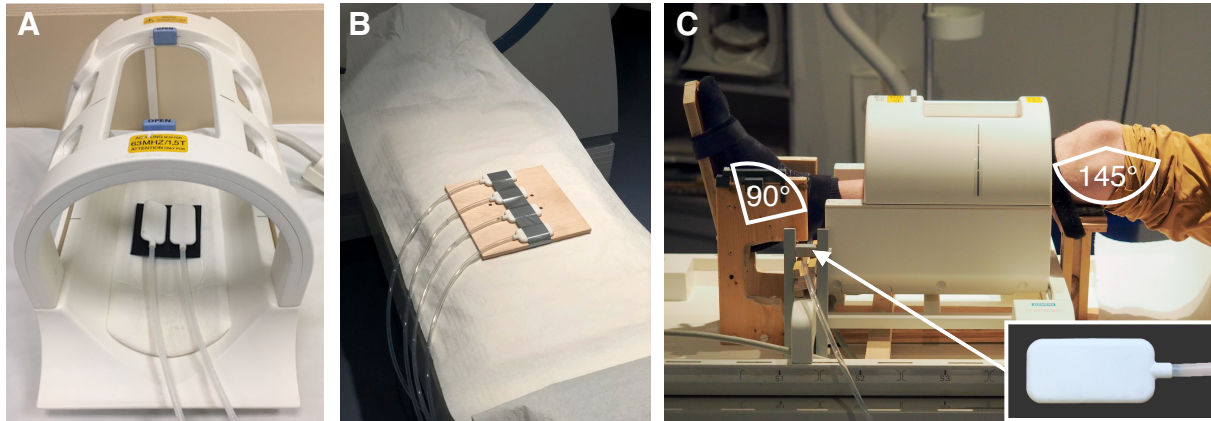
Figure 3. Pneumatic actuators were placed near the target tissue. **A** For brain stimulation in Study 1[10], two actuators were positioned inside a birdcage head coil. **B** In Study 2[11], four actuators were mounted on a wooden plate and positioned under the back of the supine participant. **C** In Study 3[12], a custom-designed footplate was mounted next to a knee coil to maintain the participant's foot position during the exercise. A single actuator was placed under the participant's Achilles tendon (white arrow).

In Study 2[11], four actuators were mounted on a wooden plate positioned under the back of the supine participant and at the level of the middle thoracic spine (see Figure 3B). A transverse T2-weighted fast half-Fourier turbo spin-echo pulse sequence (time of echo [TE]: 41 ms, time of repetition [TR]: 750 ms, field of view [FOV]: 360×250 mm²) was used to place the sagittal MRE slice and measure the participant's aortic diameter.[11] In three successive experiments, frequencies of 50 Hz, 62.5 Hz, and 80 Hz were induced. A fingertip pulse oximeter was used for cardiac triggering.

In Study 3[12], each participant was required to perform two types of exercises during successive scans: isometric plantar flexion and isometric dorsiflexion. Both exercises followed the same sequence with three distinct periods: muscle at rest for 10 s (baseline), muscle activation for 10 s (exercise), and muscle at rest for the remaining 10 s (recovery).[12] The commands to start and stop muscle activation were given via headphones. A custom-made footplate mounted on the radiofrequency (RF) knee coil was used to maintain the participant's foot position perpendicular to the lower extremity and ensure isometric muscle activation.[12] The knee was slightly flexed at an angle of approximately 145° (see Figure 3C). Additionally, hook-and-loop tape fixed the participant's foot and ankle to ensure a minimum rotation in plantar and dorsal directions.[12] During the exercise, the participants intentionally exert force on the fixed footplate through the ball of their feet without changing their position.[12] A single actuator was placed under the participant's Achilles tendon and induced vibrations at a single frequency of 40 Hz. Imaging was performed to obtain a transverse view through the center of the lower leg. A T1-weighted image (TE: 13 ms, TR: 450 ms, FOV: 160×160 mm²), which shared the slice and orientation with the MRE, was also acquired to select the region of interests (ROI).

In all three studies[10-12], a wave generator (CGC Instruments, Chemnitz, Germany) was used to store the vibration parameters and was automatically configured by the pulse sequence. The clock of the wave generator was synchronized with the MRI unit clock to avoid any mismatch between vibration excitation

and imaging. A vibration forerun of 3 s was used before image acquisition to establish a mechanical steady state in all MRE examinations.

3.4 ssMRE pulse sequence

Cardiac-gated ssMRE and stroboscopic under-sampling of harmonic vibrations

A 2D cardiac-gated gradient-echo ssMRE pulse sequence with segmented spiral k-space readout was developed.[10, 11] The multi-shot approach of ssMRE uses a cardiac trigger on which the segmented image acquisition is repeatedly synchronized. In this way, several snapshots capturing different k-space trajectories, MEG components, and frequencies are combined for a cardiac phase derived from different heartbeats. The spatial and temporal resolution is determined by the number of k-space segments and the TR, respectively. Cardiac-gated ssMRE is therefore suitable for capturing periodic processes, such as those occurring during cardiac function, with high temporal and spatial resolution. Figure 4 shows an illustration of the timing and pulse sequence of ssMRE.

Before the actual image acquisition, dummy RF excitations are applied to establish a steady-state magnetization. After the first cardiac trigger signal, the first k-space segment is acquired rapidly at a frame rate equal to the TR for all successive images covering the period of interest. After the first k-space segment has been recorded for all images, RF dummy excitation is applied again to maintain the steady-state magnetization and wait for the next trigger signal. After receiving the next cardiac trigger signal, recording of the complementary second k-space segment is initiated for all images in the same manner as above. This procedure of periodically acquiring complementary k-space segments for the series of images is repeated until the entire k-space is recorded. Each TR includes RF excitation, MEG, k-space readout, and signal spoiling. Amplitude strength and length of the MEG are identical for all frequencies and shorter than the respective wave period according to the principle of fractional encoding.[26] The spiral k-space trajectories start in the center of k-space. The first image from the image series is recorded without motion encoding and used as a static signal phase to perform voxel-wise phase corrections in all subsequent images. For this purpose, the signal phases of the subsequent images are rotated based on the static signal phase. The phase correction removes the static phase offsets and, thus, improves the performance of the phase unwrapping algorithm.[10] After the entire k-space has been recorded for all images, image acquisition is repeated for the remaining orthogonal MEG components and frequencies.

The rapid image acquisition of ssMRE combined with continuous vibrations allows for controlled aliasing in the encoding of the time-harmonic displacements. Here, a well-defined TR corresponding to the vibration period allows for the acquisition of distinct time points of the wave cycle within the successive image series itself. This approach is henceforth termed stroboscopic under-sampling of harmonic vibrations (SUV).[12] To ensure that the wave phases between repetitive scans match, the time delay is synchronized in real-time immediately after the cardiac trigger and before image acquisition. An example is shown in Figure 4A, the TR of 40 ms was intentionally mismatched to the vibration period of 50 ms (20 Hz), so that five consecutive images capture a complete wave cycle without the need for further repetitions.[10] A complete series of images thus captures several complete wave cycles.

In Study 2[11], a pencil beam respiratory navigator was used to correct the slice position between the k-space segments to adjust for respiratory movement. The corresponding figure for the aorta examination used in Study 2[11] is in the Appendix (Figure A-1).

Details of the pulse sequence parameters are given in Table 2.

A   Synchronization

Cardiac trigger

Cardiac cycle

Continous harmonic vibration at 20 Hz

RF excitation

Synchronization

20-Hz period = 50 ms

TR = 40 ms

Stroboscopic under-sampling of harmonic vibrations (SUV)

1 2 3 4 5 6 7 8 9 ... 98 99 100

0 40 80 120 160 200 240 280 320 ... 3880 3920 3960

Time (ms)

B   Sequence diagram

Continous harmonic vibration at 20 Hz

RF excitation   25°   25°   25°

G_X readout

G_Y phase-encoding

G_Z slice-select 0th mn MEG 0th mn MEG 0th mn MEG

Analog-to-digital conversion (ADC)

0   20   40   60   80   100   120

Time (ms)

C   Repetitions

Cardiac phases   trigger + sync.   trigger + sync.   trigger + sync.

1 2 3 4 5 6 7 8 9 100   1 2 3 4 5 6 7 8 9 100   1 2 3 4 5 6 7 8 9 100

k-space segments   1   2   ...   9

MEG components   Slice-select   Readout   Phase-encoding

Frequencies   20 Hz   31.25 Hz   40 Hz

Figure 4. Cardiac-gated ssMRE sequence used for the brain examination in Study 1 [10]. **A** Cardiac signal and continuous vibrations are continuously monitored. Radiofrequency (RF) excitation is consistently applied to maintain the steady-

state of magnetization. When a cardiac trigger is detected, a delay is inserted to achieve synchronization with the desired vibration phase, and then 100 images are quickly acquired. The time of repetition (TR) of 40 ms is intentionally not synchronized to the vibration period of 50 ms. With this time offset of 10 ms, different wave phases can be captured successively so that a complete wave cycle can be sampled within five TRs. **B** Gradient-echo-based spiral readout and low flip angle excitation enable to acquire multiple images and sample multiple wave phases within a cardiac cycle. The duration of the motion encoding gradients (MEG) and the readout determine the temporal resolution. **C** Cardiac triggering, vibration synchronization, and image acquisition are then repeated for nine k-space segments to complete the k-space. The spatial resolution can be adjusted by the number of acquired k-space interleaves. MRE is repeated to capture all three orthogonal MEG components and three frequencies.

Real-time ssMRE

ssMRE with SUV has been extended to a single-shot rtMRE variant with interlaced MEG image acquisition that allows for real-time quantification of viscoelastic properties (see Figure 5).[12] rtMRE derives viscoelasticity maps from a single measurement and, thus, can also measure dynamic non-periodic effects. Two in-plane orthogonal MEG components are continuously recorded in an interlaced fashion, resulting in a total MRE frame rate of 2 times TR.[12] The interleaved arrangement of the MEGs allows us to acquire multiple MEG components in a single MRE experiment. The first image of the image series for both in-plane MEG components is taken without motion encoding and is used to perform voxel-wise phase corrections, similar to those performed for ssMRE. A single vibration frequency is applied continuously throughout the experiment. Due to the acquisition of only a single readout in rtMRE for each image and, thus, no repetitive scans, neither a trigger signal nor synchronization of the vibration phase is required. This makes any MRI and wave generator clock synchronization unnecessary. As shown in Study 3[12], 30 s of rtMRE image acquisition yields 30 s viscoelasticity maps, with a frame rate equal to the 2 times TR used. Pulse sequence parameter details for rtMRE can be found in Table 2.

A Synchronization

Continous harmonic vibration at 40 Hz

Image acquisition with interleaved MEGs

|↔| 40-Hz period = 25 ms

|←——→| TR = 85 ms

Interleaved stroboscopic under-sampling of harmonic vibrations (SUV)
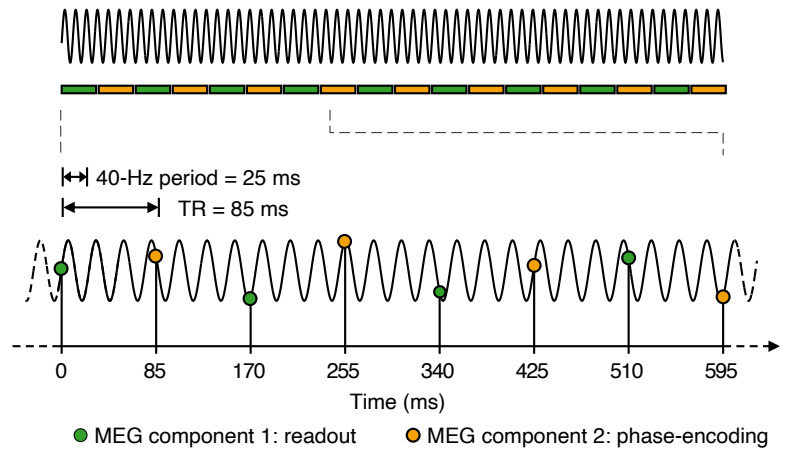
Time (ms)
0   85   170   255   340   425   510   595

● MEG component 1: readout   ● MEG component 2: phase-encoding

B Sequence diagram

Continous harmonic vibration at 40 Hz

25°   25°

RF excitation

$0^{th}+1^{st}$ mn MEG

G_X readout

$0^{th}+1^{st}$ mn MEG

G_Y phase-encoding

G_Z slice-select

Analog-to-digital conversion (ADC)

Time (ms)
0   20   40   60   80   100   120   140   160
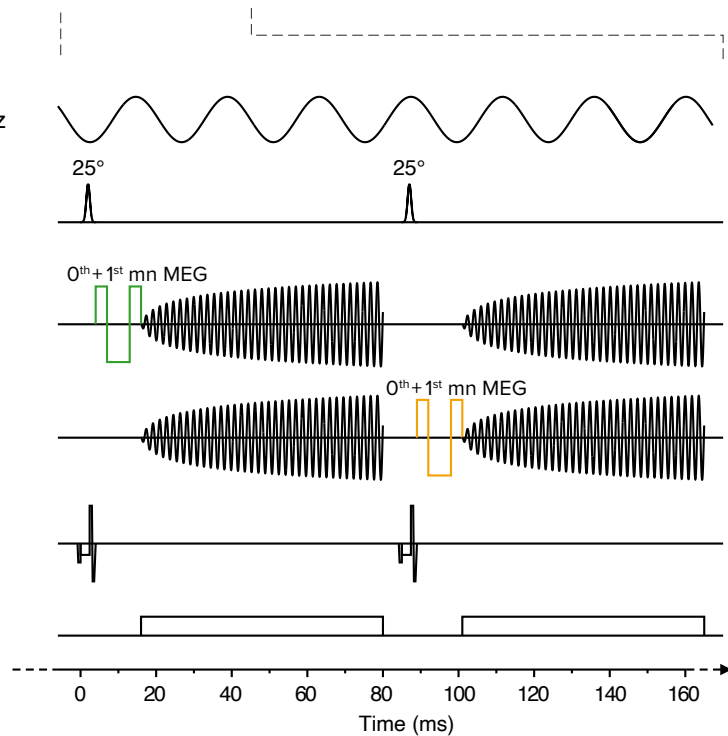
Figure 5. rtMRE sequence with interleaved motion-encoding gradient (MEG) image acquisition used in Study 3[12]. **A** Compared to the multi-shot ssMRE, the single-shot rtMRE requires no triggering and no synchronization with the vibration phase. Radiofrequency (RF) excitation was consistently applied to maintain the steady-state magnetization. Following the SUV principle, the time of repetition (TR) of 85 ms was intentionally chosen with respect to the vibration period of 25 ms to capture different wave dynamics successively. Orthogonal in-plane MEG components were acquired in an interleaved manner to avoid repeated measurements. **B** Like ssMRE, gradient-echo spiral readout and low flip angle excitation, allows to acquire multiple images and sample multiple wave phases at a high frame rate.

Table 2. Pulse sequence details.[10-12] MEG: motion-encoding gradient.

	Study 1 [10]	Study 2 [11]	Study 3 [12]
TE (ms)	20	12	16
TR (ms)	40	35	85
Frame rate (Hz)	25	28.6	5.9
Number of images (period [s])	100 (4)	32 (1.1)	360 (30.6)
Number of spiral trajectories	9	5	1
Matrix size	192×192	192×192	128×128
Voxel size (mm^3)	1.1×1.1×5.0	2.1×2.1×5.0	1.25×1.25×5.00
Field of view (FOV; mm^2)	220×220	400×400	160×160
Flip angle	25°	15°	25°
MEG components	3	3	2 (in-plane)
MEG waveform	0th mn	0th + 1st mn	0th + 1st mn
MEG strength (mT/m)	30	35	35
MEG period (ms)	15	11	12
Frequencies (Hz)	20, 31.25, 40	50, 62.5, 80	40
Complete scan time (min)	~8*	~5*	0.5

* Depending on the heart rate.

3.5 Time-resolved viscoelastic parameter reconstruction

We adapted the parameter reconstruction to the SUV displacement encoding strategy in order to reconstruct time-resolved parameter maps.[10] First, as in conventional reconstruction, raw phase signal images were denoised by a Gaussian kernel with sigma 0.65 pixels and then unwrapped. Afterward, we replaced the temporal FFT with a temporal Hilbert transformation. The conventional FFT approach would result in the entire image series being averaged to produce a single complex wave image; any temporal information would be lost. By contrast, the Hilbert transform extracts the induced fundamental frequency through a Gaussian bandpass, resulting in complex wave images for each acquired image and timepoint.[10] Figure 6 shows representative examples of complex-valued wave images for each study. Further reconstruction was done according to the standard pipelines for either MDEV or *k*-MDEV.

In Study 1 [10], 99 complex-valued wave images were inverted according to the MDEV algorithm (the first of the 100 images acquired was used for phase correction of all subsequent images but not for data analysis). As a result, we obtained 99 maps of stiffness and fluidity in terms of $|G^*|$ and φ respectively, covering 4 s of CAP with a frame rate of 25 Hz.[10]

In Study 2[11], we used a dual reconstruction pipeline to invert all 32 complex-valued wave images. Here the *k*-MDEV algorithm was used to reconstruct the SWS as a stiffness surrogate, while the MDEV algorithm was used to reconstruct the fluidity with respect to φ. As a result, we obtained 32 stiffness and fluidity maps covering 1.1 s with a frame rate of 28.6 Hz.[11]

In Study 3[12], we first performed image registration with the open-source toolbox Elastix[27] to account for slight movements of the lower leg during the exercise. Thereby, all 360 real and imaginary parts of the complex MR signal were transformed based on the corresponding magnitude using rigid in-plane transformation.[12] The two motion-corrected MEG components were then separated and further processed using the dual pipeline, as described in Study 2[11]. The result was 180 maps of SWS and φ, which displayed 30.6 s of dynamic exercises at a frame rate of 5.9 Hz.[12]
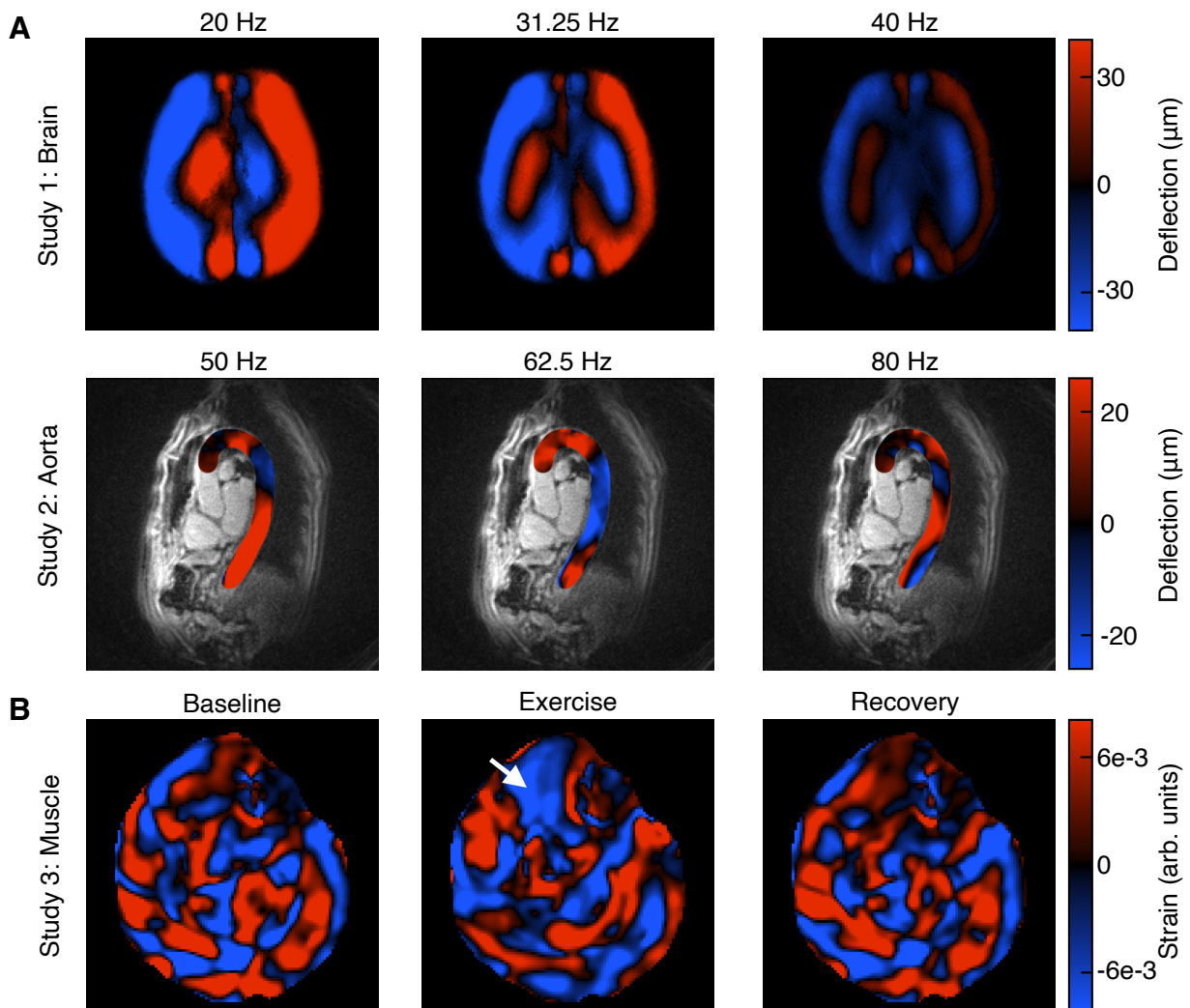
Figure 6. A Example wave images of three frequencies after denoising, unwrapping, and temporal Hilbert transformation in the brain (transversal view) and aorta (sagittal view).[10, 11] **B** Example wave images (in-plane curl) at 40 Hz in the lower leg extremity of three representative stages (baseline, exercise, and recovery) of dorsiflexion.[12] The white arrow shows an increase in shear wavelength in the TIBA as a result of muscle activation.

3.6 Parameter analysis and statistical tests

Time-dependent viscoelastic parameters were analyzed in the context of ROIs. An SNR analysis[28] was performed in all three studies[10-12] to test the signal stability of MRE-derived parameters and wave amplitudes over the course of recording. Statistical significance was assumed at $p < .05$. In studies 1[10] and 3[12], errors are reported in standard deviation. In Study 2[11], errors are given in interquartile range and interclass correlation coefficients (ICC) are reported with 95% confidence interval (CI).

In Study 1[10], the entire brain parenchyma was analyzed, except for the lateral ventricles and larger sulci. Time-resolved maps of $|G^*|$ and φ were spatially averaged within the ROI of the brain parenchyma and correlated with the CAP signal.[10] The CAP time course was derived from a modulation of the signal magnitude of ssMRE within region of pulsating temporal arteries in subcutaneous tissue.[10] Here, the influx of fresh blood with completely relaxed magnetization properties led to a periodically increased signal intensity during the passage of the arterial pulse wave (see Figure 7).[10] Cross-correlation of the viscoelastic parameters and the CAP signal was performed to obtain correlation coefficients and time lag information.[10] The slope of the time-shifted time courses of stiffness and fluidity versus CAP was calculated for each participant assuming a linear model. Afterward, a one-sample two-tailed t-test was used to test, whether the slopes significantly differed from zero for all participants. The average effect sizes of $|G^*|$ and φ between diastole and systole were determined by manually selecting the cardiac phases based on the CAP signal.[10] Assuming normally distributed data residuals (Shapiro–Wilk normality test, $p = .49$), a two-tailed paired t-test was used to test whether $|G^*|$ and φ vary significantly during the different cardiac phases.[10]
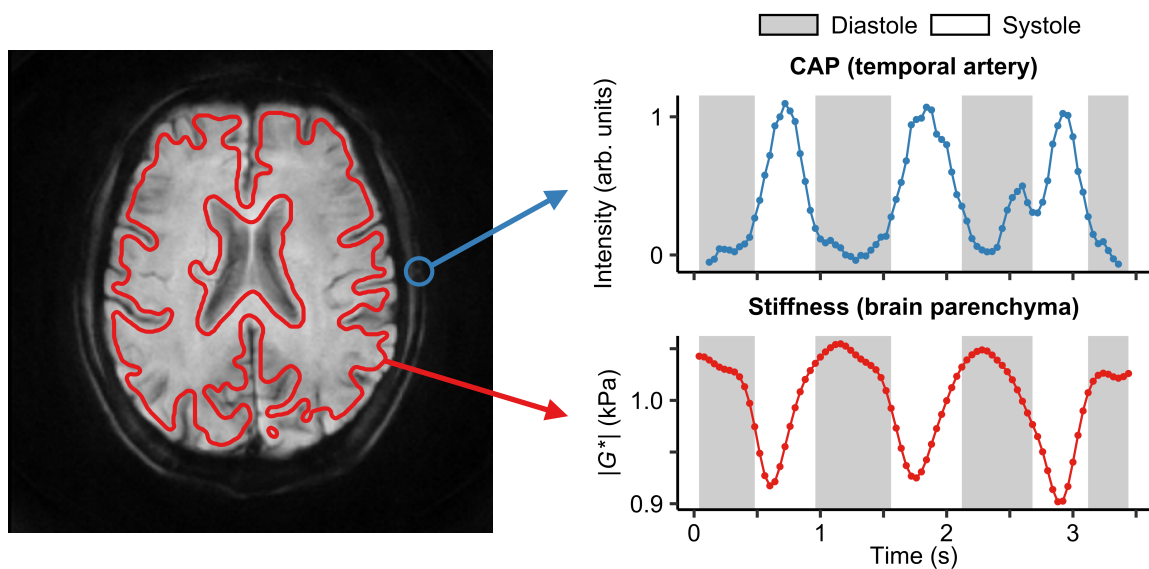
Figure 7. Representative ssMRE signal magnitude in transverse view with the delineated ROIs for brain parenchyma (red) and temporal arteries (blue) and corresponding spatially-averaged time courses of cerebral arterial pulsation (CAP) and stiffness.[10]

In Study 2[11], viscoelastic parameters were analyzed in three aortic sections: AA (aortic root to the brachiocephalic trunk), AD (distal to the origin of the left subclavian artery to the aortic hiatus), and AAb

(between the aortic hiatus and the aortic bifurcation). Figure 8A shows a representative example of the three segments. The waveguide effect allows for the wall stiffness to be estimated by placing an ROI covering both the aortic wall and the lumen.[11] While shear waves generally cannot penetrate fluids, the principle of the waveguide effect is that the aortic wall and the adjacent blood of the aortic lumen have the same spatial and temporal displacement in response to the induced vibrations.[11] Temporally resolved maps of SWS and φ were spatially averaged for each aortic segment and evaluated during diastole.[11] Systolic MRE-derived parameters were not evaluated because the systolic pulse wave corrupted the steady-state of magnetization and caused a major decrease in the SNR of the ROIs (see Figure 8B).[11] Spatially and diastolic averaged SWS and φ values of the aortic segments were tested for significant differences using the Kruskal Wallis test.[11] A pairwise comparison was then performed using the Wilcoxon rank-sum test. Inter-reader agreement was evaluated by two readers, both blinded to the participant's data. For reproducibility, repeated measurements of seven participants were analyzed, each of which was performed 1 h after the first measurement.[11] Between measurements, the participants rested in a sitting position to maintain comparable blood pressure and PWV values.[11] ICCs were calculated to test for inter-reader and intra-reader agreement and reproducibility.[11] Linear regression analysis was performed to test for correlations with age, sex, BMI, vessel diameter, blood pressure, PWV, and SWS.[11] In case of a significant interaction, a multivariate analysis was performed using a general linear model and Akaike information criterion. As φ is more susceptible to noise than SWS, it was excluded from the regression analysis.[11]

A

B
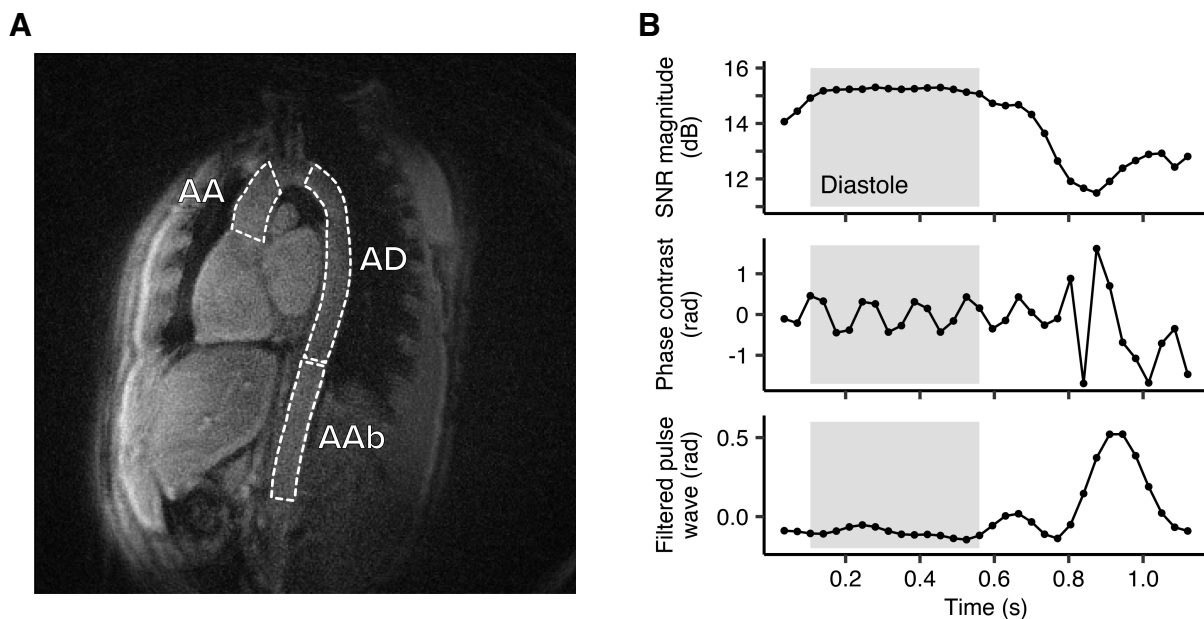
Figure 8. A Three aortic segments were examined in a sagittal view: ascending thoracic (AA), descending thoracic (AD), and abdominal (AAb) aorta.[11] **B** During diastole (highlighted in gray) the signal to noise ratio (SNR) remains stable, the wave encoding can be depicted clearly, and there is no interference from the passing pulse wave.[11]

Study 3[12] analyzed the time courses of the SWS and φ parameters in the six different muscle groups of the lower leg: GAST, SOL, PER, EXT, TIBA, and TIBP. The ROIs were drawn based on a higher resolution T1-weighted image (see Figure 9). SWS and φ were spatially averaged within each ROI and

analyzed for temporal variations. For the group statistics, the time courses within each of the three exercise phases (baseline, exercise, and recovery) were further averaged over time. Here, the first and last 2.5 s of each phase were not considered to minimize inter-transient effects.[12] A linear mixed model was used to test for significant changes in SWS and φ among the three exercise phases.[12] The model treated SWS and φ as dependent variables, the three exercise phases as independent variables, and the participants as a random effect.[12] The random effect used considers the non-independence of the data points due to repeated measurements of identical participants and muscle states during the three exercise phases.[12] Multiple comparisons using Tukey's method were then used to compute p-values.
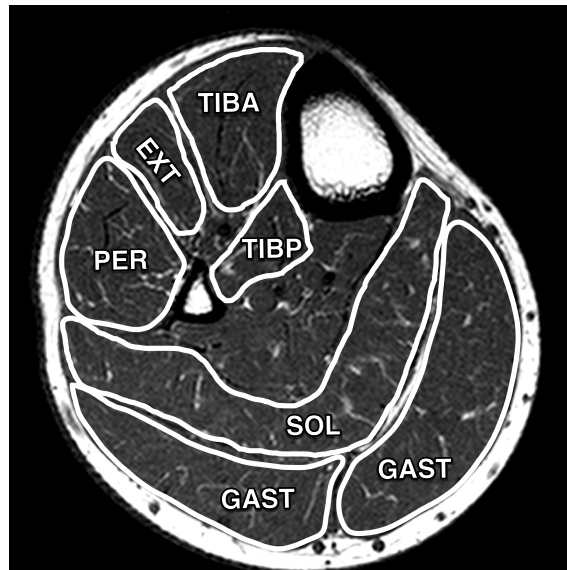
Figure 9. T1-weighted magnitude with highlighted ROIs for the six investigated muscles: gastrocnemius (GAST), soleus (SOL), peroneus (PER), tibialis posterior (TIBP), tibialis anterior (TIBA), and extensor digitorum longus (EXT). T1-weighted magnitude corresponds to the geometry and orientation from the MRE.[12]

4 Results

4.1 Study 1: Effect of CAP on brain viscoelasticity

Group-mean SNR time courses for the signal magnitudes (16.5 ± 0.9 dB) and the shear wave amplitudes (12.0 ± 4.1 dB) exhibit no significant changes over the acquisition period.[10] Total group-mean shear wave amplitudes were 35.6 ± 6.8 μm.[10] Figure 10 shows representative maps of stiffness and fluidity, which were averaged over the entire acquisition window.

In all participants, compared with that of cerebral diastole, we found a significant decrease in stiffness during cerebral systole of -6.6 ± 1.9% or -56 ± 22 Pa ($p < .001$).[10] Average stiffness values in terms of $|G^*|$ were 826 ± 157 Pa for diastole and 770 ± 141 Pa for systole (Figure 11A).[10] Figure 12 shows three representative examples of time courses of the CAP signal and corresponding relative stiffness. Time courses of CAP and stiffness were found to be significantly inversely correlated, with a mean normalized linear slope of -1.2 ± 0.6 ($p < .001$).[10] Cross-correlation analysis showed no significant difference in time lag between CAP and stiffness from zero (40 ± 100 ms, $p = .18$).[10] In addition, compared with that of cerebral diastole, we found a weak but significant increase in fluidity during cerebral systole of 0.5 ± 0.5% or 0.006 ± 0.005 rad ($p = .002$; Figure 11B).[10] Group-mean values of fluidity were found to be 1.12 ± 0.07 rad during cerebral systole and 1.11 ± 0.07 rad during cerebral diastole.[10] The correlation of fluidity and CAP signal was found to be weak, with a mean linear slope of 0.5 ± 0.7 ($p = .03$).[10]

CAP-derived heart rates correlate significantly with measured heart rates with group-mean values of 69 ± 11 1/min and 65 ± 8 1/min, respectively ($r = .8$, $p = .002$).[10] No age effect was found in the CAP-rate ($r = -.19$, $p = .55$).[10] Group-mean periods of CAP-derived systole and diastole were 287 ± 105 ms and 610 ± 150 ms, respectively.[10]

Figure 11C shows a moderate reduction in the effect of systolic stiffness decrease with age with 0.10 ± 0.05% relative effect size per year ($r = -.59$, $p = .042$).[10] By contrast, no significant correlation between the fluidity effect size and age was found ($r = .14$, $p = .66$).[10] No significant influence of stiffness or fluidity on blood pressure was observed.[10]
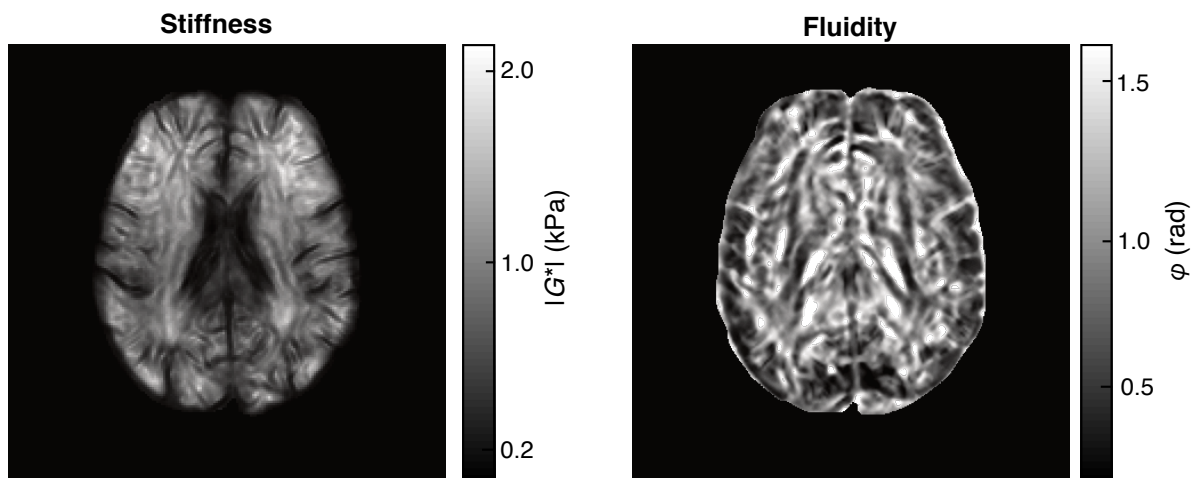
Figure 10. Temporally averaged ssMRE-derived maps of stiffness ($|G^*|$) and fluidity (φ; each averaged over all 99 images).[10] The stiffness map, in particular, reveals the spatial orientation of prominent white matter tracts with higher intensities.[10]
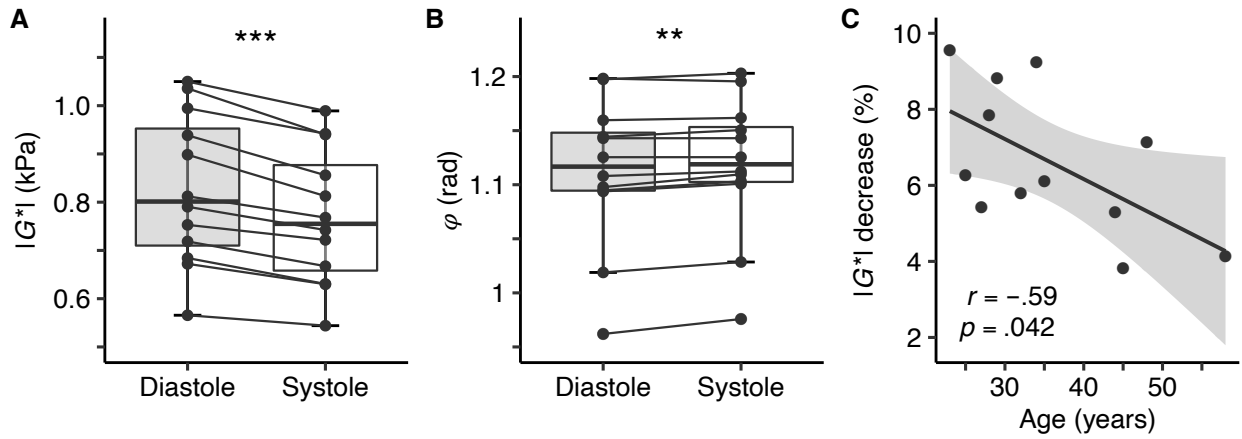
Figure 11. Statistics on the influence of cerebral arterial pulsation (CAP) on the viscoelasticity of the brain.[10] Group-mean stiffness ($|G^*|$), **A**, and fluidity (φ), **B**, of the brain parenchyma in diastole (gray) and systole (white) across all participants with individual values and quartiles (*$p < .05$, **$p < .01$, ***$p < .001$). **C** Linear correlation of the average relative changes in stiffness induced by CAP as a function of age (gray areas indicate confidence intervals).
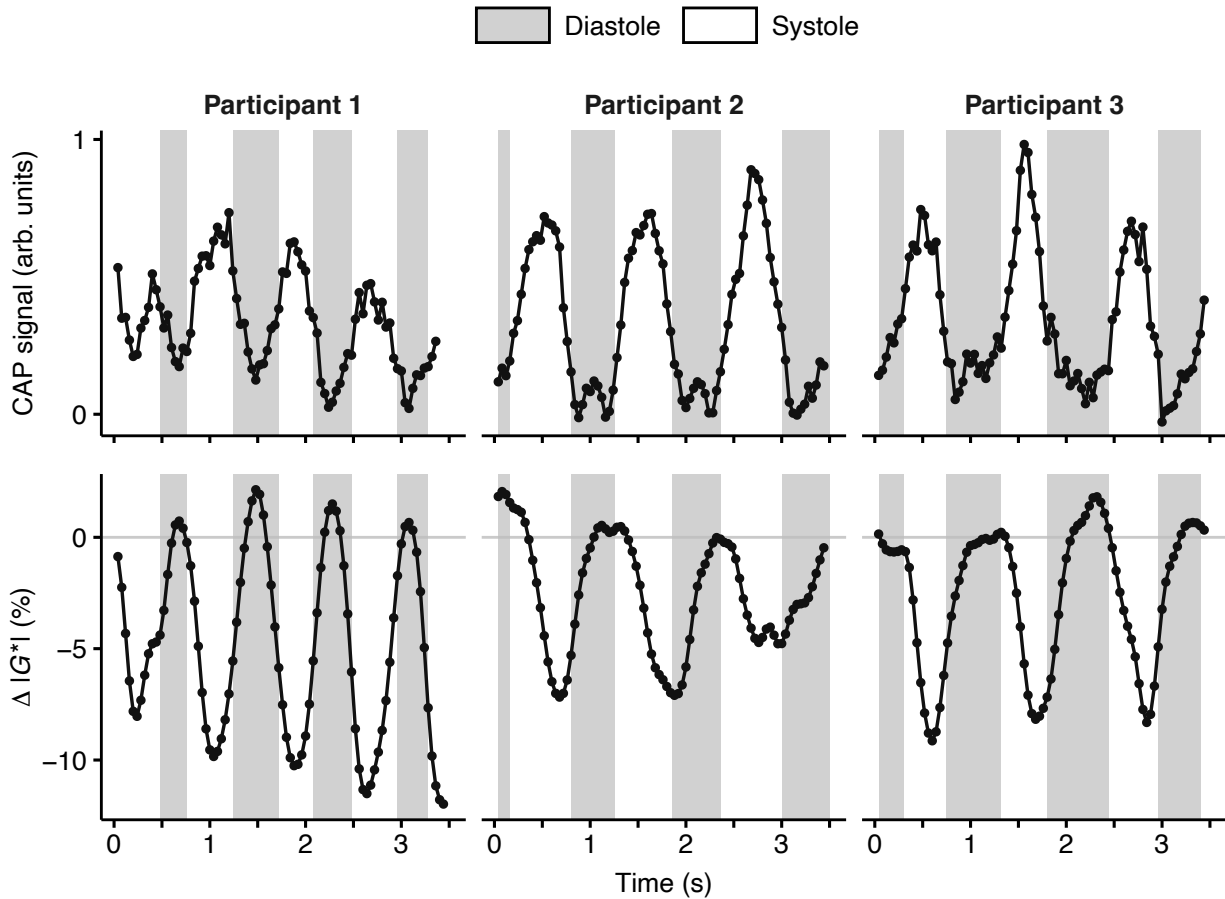
Figure 12. Representative spatially averaged time courses of normalized cerebral arterial pulsation (CAP) and changes in relative stiffness ($|G^*|$) in three participants.[10] The zero baseline for the relative stiffness is defined as the average diastolic stiffness, which was temporally assigned by the CAP signal (shaded gray).

23

4.2 Study 2: Viscoelasticity of the thoracic and abdominal human aorta

No significant changes in SNR of the MRE signal magnitudes (13.6 ± 1.5 dB) and shear wave amplitudes (52.3 ± 2.8 dB) within the diastolic period were observed over time.[11] Group-mean shear wave amplitudes were 20.7 ± 3.7 μm.[11]

In all participants, we found significantly lower median stiffness values in AA, with 1.6 ± 0.2 m/s, than those of AD, with 2.4 ± 0.3 m/s ($p < .001$), and AAb, with 2.5 ± 0.6 m/s ($p < .001$).[11] No significant difference was found between AD and AAb ($p = .67$).[11] Figure 13 shows two representative stiffness maps of two participants of different ages. Group-median fluidity values were determined with AA fluidity found to be 0.92 ± 0.06 rad, AD, 0.90 ± 0.12 rad, and AAb, 0.81 ± 0.15 rad.[11] The fluidity values of AAb and AA were significantly different ($p = .02$); no further significant difference was found.[11]

Age ($R^2 = .08$, $p < .001$), PWV ($R^2 = .08$, $p = .001$), and the aortic diameter ($R^2 = .06$, $p = .005$) showed a significant correlation with the measured stiffness values.[11] By contrast, no significant correlation with stiffness was found for BMI ($R^2 = -.007$, $p = .72$), blood pressure ($R^2 = -.001$, $p = .38$), and sex ($R^2 = -.008$, $p = .86$).[11] In addition, a multiple linear regression analysis was performed taking into consideration age, reader, and aortic diameter.[11] The best model demonstrated a weak but significant influence of age on the stiffness values for AA ($R^2 = .23$, $p = .005$), AD ($R^2 = .28$, $p < .001$) and AAb ($R^2 = .38$, $p < .001$; see Figure 14).[11] Aortic diameter and reader showed no significant effects.[11]

ICCs was found to be excellent with 0.981 (all 95% CI, 0.952–0.992) in AA, 0.982 (0.956–0.993) in AD, and 0.991 (0.978–0.996) in AAb for interreader agreement, and 0.989 (0.958–0.996) in AA, 0.992 (0.981–0.997) in AD, and 0.998 (0.996–0.999) in AAb for intrareader agreement.[11] Reproducibility analysis revealed ICCs of 0.957 (all 95% CI, 0.792–0.992) in AA, 0.970 (0.85–0.995) in AD, and 0.969 (0.851–0.994) in AAb.[11]
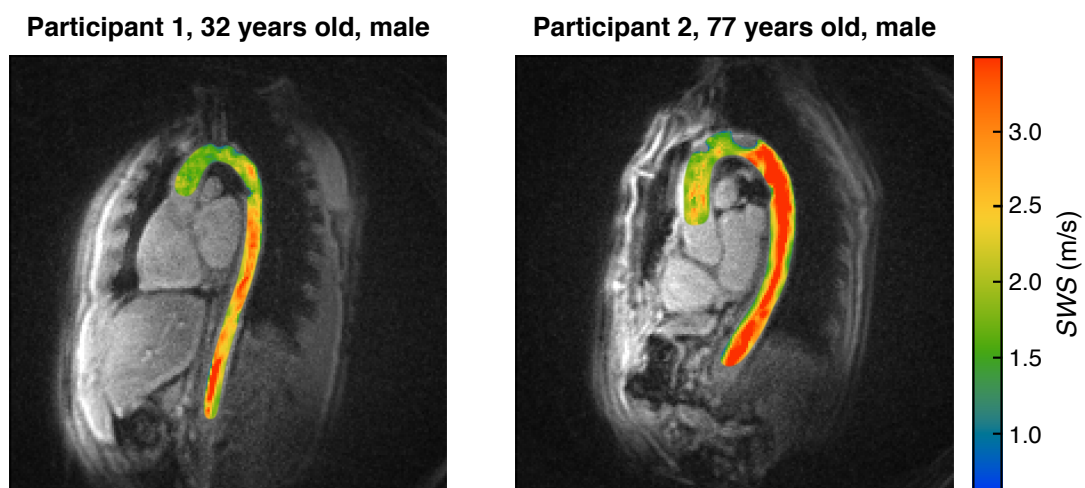
Figure 13. Representative maps of diastolic stiffness (SWS) of the aorta in sagittal view of two participants of different ages.[11]
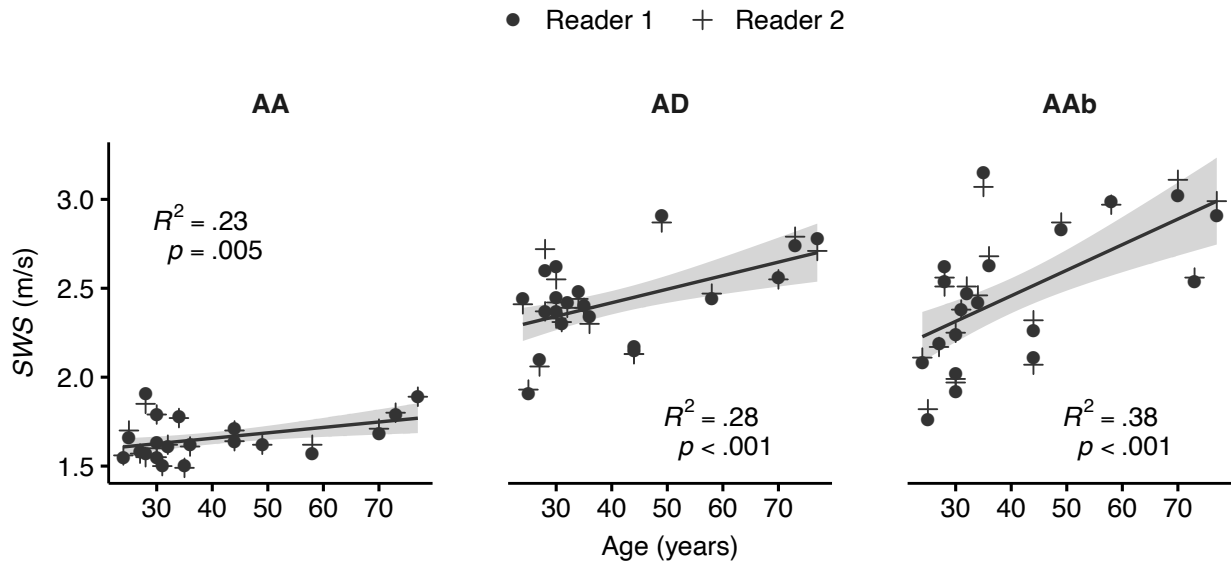
Figure 14. Stiffness (*SWS*) values for both readers as a function of age in the three aortic segments investigated: ascending aorta (AA), descending aorta (AD), and abdominal aorta (AAb).[11] The regression analysis shows a weak but significant influence of stiffness, pooled from both readers on age, with higher values in older individuals. The observed influence of age on stiffness increases from the proximal to distal aorta. No significant influence of the two readers was found. Gray areas indicate confidence intervals.

4.3 Study 3: Real-time viscoelasticity mapping in skeletal muscle during dynamic exercises

The group-mean SNR for the MRE signal magnitudes averaged over all ROIs changed during both plantar flexion and dorsiflexion approximately 3% identically from baseline, 12.5 ± 2.0 dB, to exercise, 12.9 ± 2.0 dB, to recovery, 12.6 ± 2.0 dB ($p < .001$).[12] The SNR for the displacement amplitudes changed approximately 2% from baseline, 54.3 ± 2.5 dB, to exercise, 55.5 ± 2.5 dB, to recovery, 54.4 ± 4.0 dB, only during plantar flexion ($p < .01$).[12] Group-mean shear-wave amplitudes were 43.2 ± 14.7 μm.[12]

Figure 15 shows representative stiffness and fluidity maps of one participant in all three phases for both exercises. The stiffness maps show obvious and distinct muscle activation patterns during both exercises.[12] During active plantar flexion, a clear and significant increase in stiffness can be observed in the area around the SOL muscle.[12] During dorsiflexion, a significant increase in the stiffness of the TIBA muscle can be observed.[12] By contrast, the fluidity maps do not show a clear activation pattern.[12]

Figure 16 shows the group-mean time courses for stiffness and fluidity, demonstrating significant increases in several muscles from baseline to exercise. As a result of plantar flexion, stiffness increased significantly in two muscles: SOL (20.0 ± 3.6% $p < .001$) and GAST (9.0 ± 6.0%, $p = .026$); and fluidity significantly increased in five muscles: GAST (13.5 ± 6.1%, $p = .004$), PER (14.3 ± 10.4%, $p = .003$), SOL (41.3 ± 12.0%, $p < .001$), EXT (8.2 ± 4.5%, $p = .043$), and TIBP (12.3 ± 4.5%, $p = .021$).[12] By contrast, there was a significant increase in stiffness due to dorsiflexion in four muscles: EXT (14.2 ± 5.2%, $p < .004$), GAST (15.4 ± 10.2%, $p < .001$), SOL (6.3 ± 2.4%, $p < .003$), and TIBA (41.5 ± 10.2%, $p < .001$); and fluidity increased significantly in five muscles: EXT (27.7 ± 0.7%, $p = .001$), GAST (15.3 ± 5.6%, $p < .001$), SOL

(17.2 ± 6.4%, $p < .001$), TIBA (27.9 ± 2.8%, $p < .001$), and TIBP (21.8 ± 2.8%, $p < .001$).[12] No significant differences were found between baseline and recovery for stiffness and fluidity.[12]
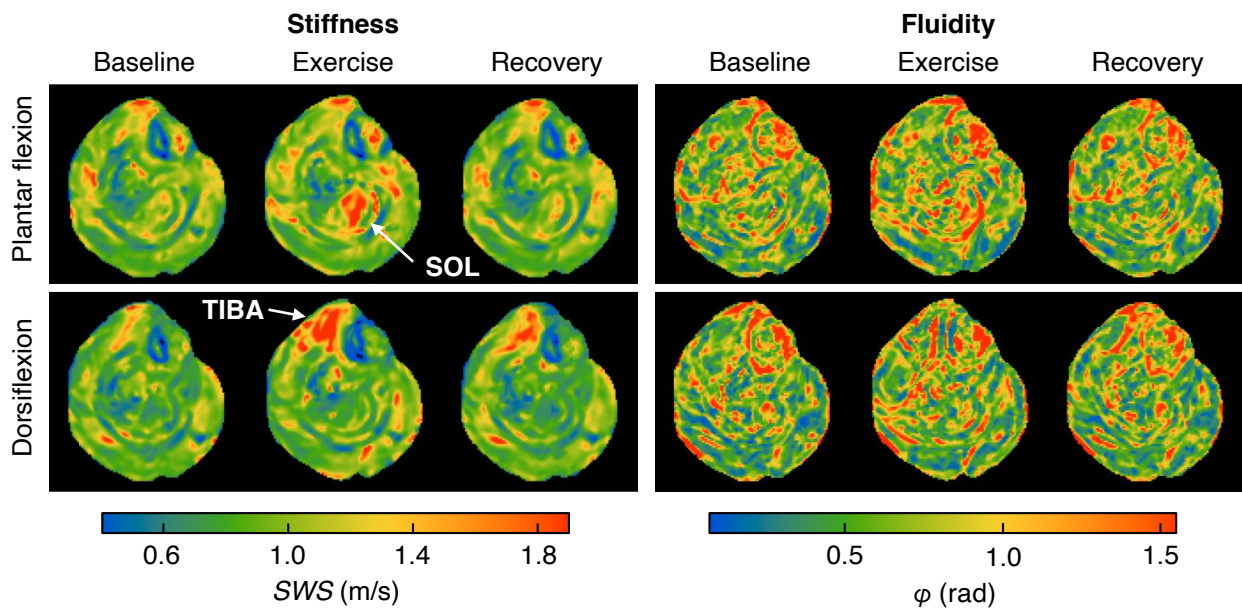
Figure 15. Representative rtMRE stiffness (SWS) and fluidity (φ) maps of the lower extremity of one participant during both exercises.[12] The stiffness maps, in particular, show a clear muscle activation pattern with a substantial increase in SWS values in the soleus (SOL) and tibialis anterior (TIBA) during plantar flexion and dorsiflexion, respectively (see white arrows).
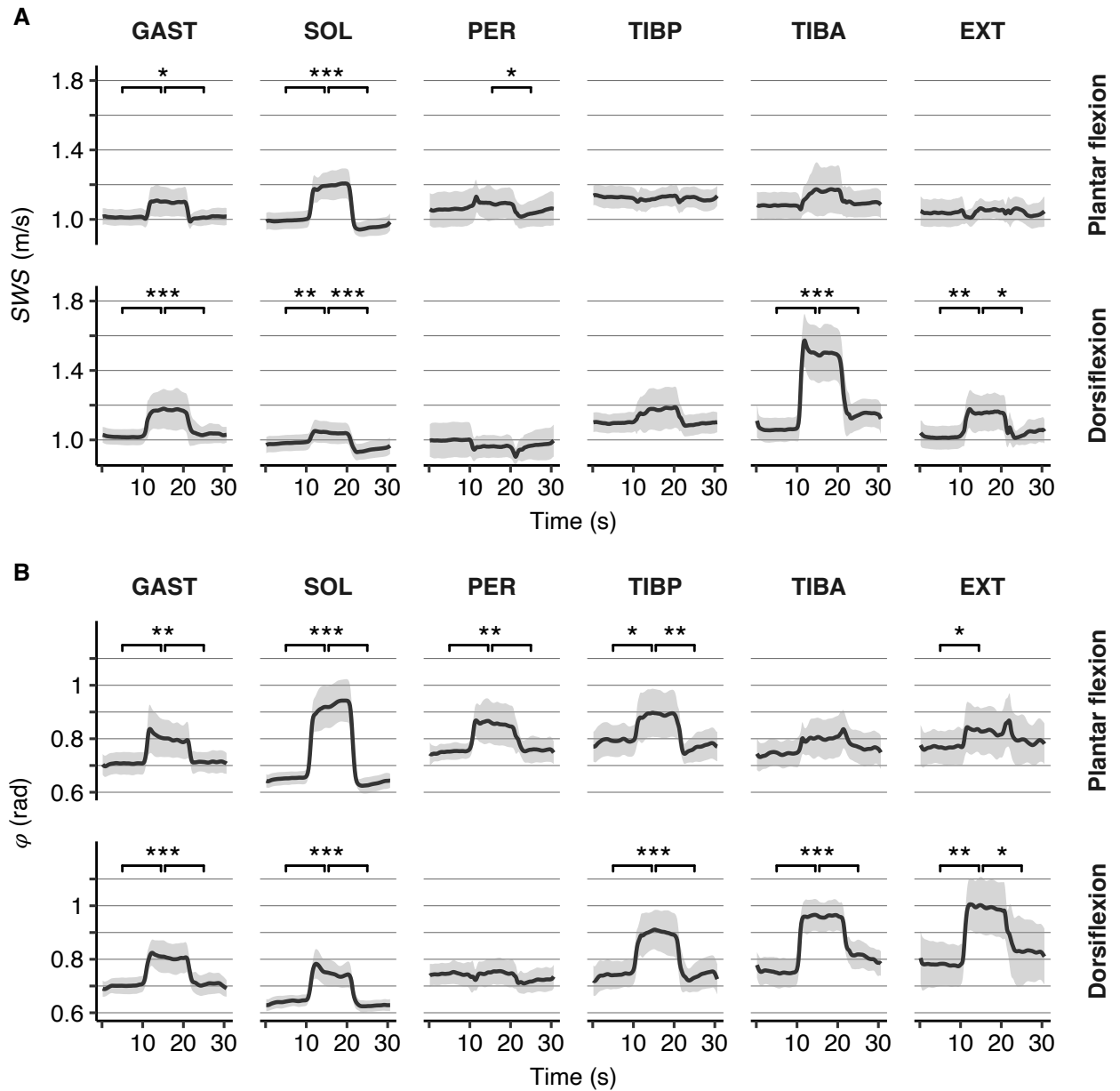
Figure 16. Time courses of group-mean stiffness (SWS) and fluidity (φ) in the gastrocnemius (GAST), soleus (SOL), peroneus (PER), tibialis posterior (TIBP), tibialis anterior (TIBA), and extensor digitorum longus (EXT).[12] Gray areas indicate group confidence intervals and asterisks demarcate significant changes between the muscle conditions (*$p < .05$, **$p < .01$, ***$p < .001$).

5 Discussion

Until now, long image acquisition times, on the order of minutes, have limited the ability of MRE to examine moving organs and capture dynamic processes. The presented methods of ssMRE and rtMRE enable, for the first time, rapid time-resolved viscoelasticity mapping. The method of ssMRE uses a steady-state of magnetization and continuous harmonic vibrations under which the fast segmented image acquisition is synchronized on a cardiac trigger. This method is combined with SUV for consecutive displacement encoding with adapted post-processing. ssMRE was applied to the human brain and aorta to demonstrate the feasibility of spatially and temporally high-resolved viscoelasticity imaging.[10, 11] Single-shot rtMRE adopts a non-segmented approach with interleaved MEG image acquisition to enable real-time viscoelasticity mapping. This approach makes vibration synchronization redundant. rtMRE was demonstrated to study dynamic and non-repeatable viscoelasticity changes in muscles of the lower extremity.[12]

As demonstrated in Study 1[10], the developed cardiac-gated ssMRE enables the imaging of the rapid interaction of CAP and the viscoelastic in vivo parameters of the human brain over the entire cardiac cycle. The results suggest that the brain parenchyma becomes significantly softer and more viscous during cerebral systole.[10] This short-term softening might be explained by the CAP-driven increase in the fluid fraction due to arterial expansion and increased blood volume during the passage of the pulse wave.[10] This poroelastic interpretation is also supported by a recent study that reported an inverse correlation between MRE-derived stiffness and cerebral blood flow in deep gray matter of the human brain.[29] This vascular-solid poroelastic effectiveness suggests that, in accordance with our hypothesis, the ssMRE may be sensitive to cerebral vascular compliance, an important clinical biomarker for brain function.[30] It was also found that the observed softening effect decreases with age.[10] A possible explanation is a lower cerebral vascular compliance in older individuals.[10] It is known that cerebral vascular compliance decreases with age as elastin loses its functionality, resulting in stiffer, less compliant cerebral arteries.[31] The data demonstrate consistent SNR and shear wave amplitude values over the acquisition period, indicating that ssMRE has stable steady-state magnetization and vibration mechanics. The high sensitivity to vascular-solid tissue interactions makes time-resolved ssMRE of the brain a promising, sensitive diagnostic tool for the detection of cerebral vascular diseases.[10]

In Study 2[11], ssMRE also showed promising results in the cardiovascular system and allowed for the quantification of diastolic stiffness for the thoracic and abdominal aorta. The findings show that the stiffness of the aortic wall increases from the aortic root to the aortic bifurcation, with AA being significantly softer than AD and AAb.[11] Furthermore, we observed a significant decrease in fluidity between AD and AAb.[11] The observed high stiffness and low fluidity in the AAb might reflect a reduced damping of the pulse wave due to the increased solid-like behavior of the vessel wall.[11] In contrast to the AAb, the AA has a higher Windkessel capacity and more substantial pulse wave attenuation, which could correspond to the lower stiffness and higher fluidity values that were observed in the AA.[11] This observation indicates that the elastic buffer function of the aorta is mainly confined to the thoracic section.[11] Similar to our findings, an increase in stiffness from the aortic root to the bifurcation was observed using indirectly measured regional PWV.[32]

Furthermore, regression analyses showed that aortic stiffness increases with age, and this age-related stiffening is more pronounced in the proximal than distal sections.[11] This age dependency might be explained by a lower amount of elastin and collagen in the tunica media of the distal aortic segments, which is, therefore, more susceptible to age-related changes in aortic wall integrity.[33] Only a few studies have published MRE-derived viscoelastic parameters of the aorta, and they report only abdominal reference values. In agreement with our results, these MRE studies report an association between stiffness, PWV, and age in the abdominal aorta.[34, 35] To the best of my knowledge, no studies have reported MRE-derived values for in vivo human thoracic stiffness. The importance of imaging the whole aortic tree and quantifying segmental differences is supported by studies, who report that the aortic arch is the most sensitive to and shows the earliest signs of arterial aging.[36, 37] Overall, Study 2[11] demonstrates the potential of aorta segment-specific stiffness and fluidity, evaluated by ssMRE, as a quantitative biomarker for cardiovascular disease.

To the best of my knowledge, Study 3[12] is the first to report on real-time MRE-derived viscoelasticity mapping. Single-shot rtMRE enables the imaging of dynamic viscoelastic changes in different muscle groups of the lower leg extremity within a single 30-seconds scan.[12] We found distinct activations of the posterior and anterior muscles during plantar flexion and dorsiflexion, respectively.[12] In accordance with the hypothesis, we observed the antagonistic behavior of the muscles, with the most substantial effect occurring in the largest flexor muscles, SOL and TIBA.[12] It is important to note that skeletal muscles are not isotropic. Instead, they can be assumed to be transversely isotropic.[1] Therefore, we intentionally placed the image slice in a transverse view in order to capture orthogonal in-plane wave components relative to the principal axis of the muscles.[12] This allowed for the acquisition of predominantly perpendicular, slow-transverse wave modes while minimizing or eliminating the contributions of the parallel, fast-transverse wave mode.[12] Only a few MRE studies have reported on changes in perpendicular SWS during muscle activation. The observed relative stiffness changes in the SOL (~20%) and TIBA (~40%) are comparable to those of the femoral muscles (~40%) and quadriceps muscle (~30%).[38, 39] Interestingly, the activation of muscle tissue leads to a significant increase in fluidity values to above $\pi/4$, indicating predominantly fluid tissue properties.[12] This might be explained by the release of bound water from polar myosin–actin groups in sliding filaments.[12]

Although the results in all three studies[10-12] are promising, some limitations must be noted. All three studies[10-12] presented are exploratory pilot studies involving a small number of participants and covering a limited age range. While the results in healthy volunteers are promising, the diagnostic potential of ssMRE and rtMRE for disease detection remains to be determined. Future studies should include patients with, for example, impaired cerebral vascular compliance or aortic hypotension to expand upon Studies 1[10] and 2[11], respectively. The methods also have some technical limitations. The cardiac triggering was performed with a finger pulse oximeter, which has relatively high variability in timing and synchronization. A more precise electrocardiogram triggering could not be used because the strong and rapid MEGs of the ssMRE pulse sequence distort the electrocardiogram signal.[10] Future hardware solutions such as built-in heart sensors can overcome these limitations and enable more precise cardiac triggering. The introduced ssMRE approach currently only captures a single slice. However, this limitation can be overcome by using

simultaneous multi-slice excitation to image several slices in parallel.[40] The MRI unit used in the presented studies[10-12] did not support this technique. As observed in Study 2[11], the method could not image systolic aortic stiffness due to a strong signal drop during pulse wave passage. Future applications should, therefore, use enhanced flow compensation. In contrast to ssMRE, rtMRE was previously only able to capture shear waves at a single frequency, so a multi-frequency inversion could not be applied.[12] In theory, however, the SUV approach allows for the simultaneous capture of several frequencies. This could not be done at the time of the studies because the wave generator used could not excite several frequencies simultaneously. However, preliminary experiments with new MRE hardware have already proven the feasibility of multi-frequency rtMRE. Finally, the MRE inversion methods used (MDEV and *k*-MDEV) cannot fully account for the 3D nature of shear-wave fields, the heterogeneity of soft tissue, and the anisotropy and viscoelastic dispersion of the shear modulus.[10]

Most of the current technical limitations can be overcome with future MRI and MRE hardware, making ssMRE and rtMRE more widely available soon with multiple frequencies and layers. The presented methods of ssMRE and rtMRE using a steady-state, rapid displacement encoding by SUV, and adapted reconstruction algorithm are essential steps towards time-resolved MRE for diagnostic purposes. More detailed explanations and discussions can be found in the original publications.[10-12]

Future applications of time-resolved ssMRE

One of the most promising future applications of the introduced time-resolved ssMRE method is cardiac MRE. While myocardial stiffness is an essential biomarker for vital heart function, current imaging techniques lack direct quantification.[41] Cardiac MRE promises a quantitative viscoelasticity mapping of the myocardium. However, cardiac MRE is challenging due to the complex synchronization of heartbeat, respiration, image acquisition, and external vibrations, and so far, only sparse in vivo data have been reported.[9] In a preliminary study [41], we applied the cardiac-gated ssMRE method used in Studies 1[10] and 2[11] to map myocardial stiffness over the entire cardiac cycle in eight healthy volunteers. Here, the method provided elastograms with a spatial resolution of $1.6 \times 1.6 \times 5.0$ mm³ at a frame rate of 22 Hz. In all participants, we observed a significant periodic variation of myocardial stiffness in terms of SWS increasing from 1.5 ± 0.2 m/s during diastole to 2.1 ± 0.2 m/s during systole ($p = .008$, Wilcoxon-test).[41] Figure 17 shows the first results of cardiac ssMRE, including representative stiffness maps in diastole and systole, respective SWS group-means, and a diagram of stiffness versus approximated volume of the left ventricle (LV). The results show the periodic stiffening and softening of the LV wall during systole or diastole, reflecting the cardiac function.[41] In agreement with the literature, the derived stiffness versus volume diagrams indicate that the increase in stiffness precedes LV contraction, while the relaxation of myocardial stiffness precedes LV dilatation.[9] This preliminary study demonstrates the great potential of time-resolved cardiac ssMRE for non-invasive, quantitative imaging to assess cardiac work in clinical examinations.
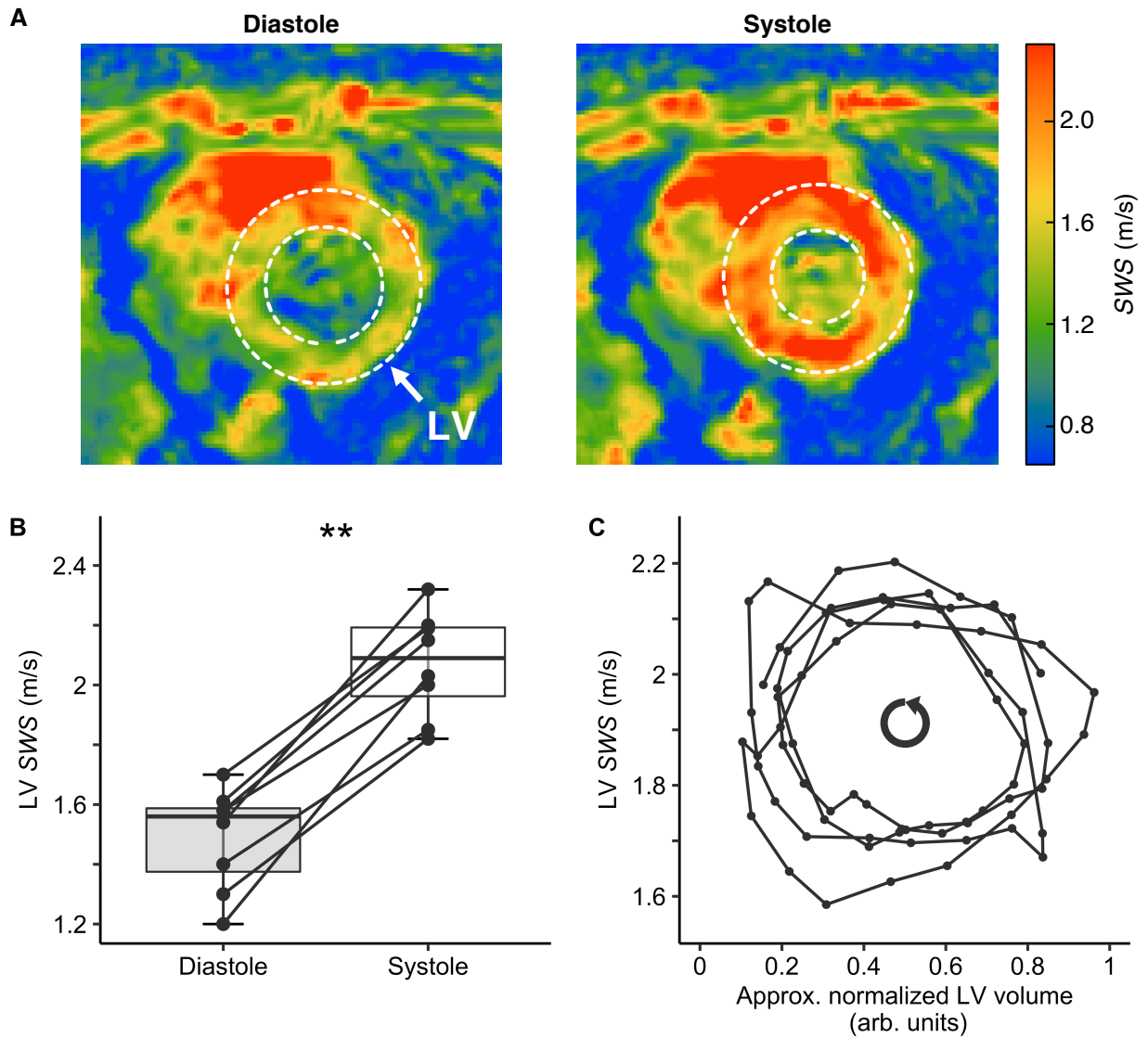
Figure 17. Preliminary results of cardiac ssMRE in eight healthy volunteers.[41] **A** Stiffness (SWS) maps in short-axis view in diastole and systole show a marked increase in left ventricular (LV) stiffness. **B** Overall changes in SWS values observed in the LV wall show an increase of $40.0 \pm 13.9\%$ from diastole to systole ($p = .008$). **C** A diagram of stiffness versus volume derived from ssMRE data reflects the mechanical work of the heart and shows that the increase in stiffness precedes the LV contraction (i.e., counterclockwise interpretation).

6 Conclusion

ssMRE and rtMRE have been introduced as versatile methods to quantify time-resolved viscoelasticity of soft tissue in vivo. Technical developments accomplished in this dissertation include a novel MRE pulse sequence, a fast displacement encoding method, and adapted parameter reconstruction for time-resolved viscoelasticity mapping. Three studies[10-12] demonstrated the feasibility of these methods for imaging viscoelastic parameters with high spatial and temporal resolution and showed their promising potential for future clinical applications.

It has been shown that the human brain parenchyma transiently becomes softer and more viscous during cerebral systole.[10] The observed effect could be explained by CAP-induced expansion of the cerebral arteries and increased blood volume.[10] Due to this sensitivity to vascular solid-tissue interactions, time-resolved ssMRE could serve as a potential biomarker to directly assess cerebral vascular compliance and related diseases.[10] Furthermore, the first reference stiffness and fluidity values were obtained for the thoracic aorta.[11] It was found that stiffness varies across different aortic segments and increases from the aortic root to the aortic bifurcation.[11] Consequently, ssMRE may be suitable to detect physiological variations and cardiovascular diseases in clinical practice.[11] Moreover, real-time viscoelasticity mapping in the lower leg muscles demonstrated distinct muscle activations during plantar flexion and dorsiflexion.[12] Specifically, the largest flexor muscles investigated (SOL and TIBA) show the most pronounced effect, with up to 40% stiffening and increased fluidity compared with baseline.[12] The ability to map changes in viscoelasticity in real-time makes rtMRE potentially useful for studying physiological processes in vivo.[12]

This dissertation contributes to the field of MRE by opening up new capabilities for studying, for the first-time, raid dynamic physiological processes with high spatial and temporal resolutions. The method developed shows excellent potential for future applications, including cardiac MRE and functional brain MRE. Time-resolved viscoelasticity mapping is a major step forward in the growing field of quantitative imaging-based biomarkers used for diagnostic purposes.

7 Author's contribution

The main objective of this doctoral project was the development of a fast, time-resolved MRE method to quantify the viscoelasticity of soft tissue during dynamic processes in vivo. Together with my supervisor Prof. Ingolf Sack and Dr. Carsten Warmuth, we initiated the technical developments in 2017. Since then, the method introduced herein has been successfully developed, extensively tested, presented at several conferences, and published in the three publications[10-12] presented to demonstrate its feasibility.

I have contributed significantly to the design, development, implementation, and communication of the method. Throughout its development, I was responsible for sequence development and validating the performance of the method using serval phantom and in vivo experiments. After developing the sequence, I intensively tested the sequence timing, optimized the sequence parameters, and adjusted the MRE hardware. I implemented the complete post-processing pipeline (including data import, filtering, and inversion) and adapted the algorithm according to the introduced Hilbert transformation to account for time-resolved viscoelasticity maps. I conceived the idea and conducted each experiment in the three publications[10-12] presented herein. For each study[10-12], I individually conducted several preliminary experiments to find the best experimental setup, vibration frequencies, and pulse sequence parameters, and to prove feasibility in general. Afterward, I performed the entire MRE parameter reconstruction and SNR analysis. Except for Study 2[11], I selected all ROIs, analyzed the reconstructed viscoelasticity maps, and completed the statistical tests of the derived results on my own. Programming was done with R, Python, and MATLAB.

Moreover, I contributed significantly to writing, editing, and revising the selected published manuscripts. I created all the figures and tables presented in publications 1[10] and 3[12]. In publication 2[11], I created Figures 2 and S2. I have created every figure and table shown in this dissertation.

References

1. Hirsch S., Braun J., Sack I. Magnetic resonance elastography: physical background and medical applications: *John Wiley & Sons*; 2017.

2. Barnes J. M., Przybyla L., Weaver V. M. Tissue mechanics regulate brain development, homeostasis and disease. Journal of Cell Science. 2017; 130(1): 71-82.

3. Glaser K. J., Manduca A., Ehman R. L. Review of MR elastography applications and recent developments. Journal of Magnetic Resonance Imaging. 2012; 36(4): 757-774.

4. Huwart L., Peeters F., Sinkus R., Annet L., Salameh N., ter Beek L. C., Horsmans Y., Van Beers B. E. Liver fibrosis: non-invasive assessment with MR elastography. NMR in Biomedicine: An International Journal Devoted to the Development and Application of Magnetic Resonance In vivo. 2006; 19(2): 173-179.

5. Singh S., Fujii L. L., Murad M. H., Wang Z., Asrani S. K., Ehman R. L., Kamath P. S., Talwalkar J. A. Liver stiffness is associated with risk of decompensation, liver cancer, and death in patients with chronic liver diseases: a systematic review and meta-analysis. Clinical Gastroenterology and Hepatology. 2013; 11(12): 1573-1584 e1571-1572; quiz e1588-1579.

6. Low G., Kruse S. A., Lomas D. J. General review of magnetic resonance elastography. World J Radiol. 2016; 8(1): 59-72.

7. Muthupillai R., Lomas D. J., Rossman P. J., Greenleaf J. F., Manduca A., Ehman R. L. Magnetic resonance elastography by direct visualization of propagating acoustic strain waves. Science. 1995; 269(5232): 1854-1857.

8. Bilston L. E., Tan K. Measurement of passive skeletal muscle mechanical properties in vivo: recent progress, clinical applications, and remaining challenges. Annals of Biomedical Engineering. 2015; 43(2): 261-273.

9. Khan S., Fakhouri F., Majeed W., Kolipaka A. Cardiovascular magnetic resonance elastography: A review. NMR in Biomedicine. 2018; 31(10): e3853.

10. Schrank F., Warmuth C., Tzschätzsch H., Kreft B., Hirsch S., Braun J., Elgeti T., Sack I. Cardiac-gated steady-state multifrequency magnetic resonance elastography of the brain: Effect of cerebral arterial pulsation on brain viscoelasticity. Journal of Cerebral Blood Flow and Metabolism. 2020; 40(5): 991-1001.

11. Schaafs L. A., Schrank F., Warmuth C., Steffen I. G., Braun J., Hamm B., Sack I., Elgeti T. Steady-State Multifrequency Magnetic Resonance Elastography of the Thoracic and Abdominal Human Aorta–Validation and Reference Values. Investigative Radiology. 2020; 55(7): 451-456.

12. Schrank F., Warmuth C., Görner S., Meyer T., Tzschätzsch H., Guo J., Uca Y. O., Elgeti T., Braun J., Sack I. Real-time MR elastography for viscoelasticity quantification in skeletal muscle during dynamic exercises. Magnetic Resonance in Medicine. 2020; 84(1): 103-114.

13. Sack I., Schäffter T. Quantification of biophysical parameters in medical imaging: *Springer*; 2018.

14. Hughes T. M., Kuller L. H., Barinas-Mitchell E. J., Mackey R. H., McDade E. M., Klunk W. E., Aizenstein H. J., Cohen A. D., Snitz B. E., Mathis C. A. Pulse wave velocity is associated with β-amyloid deposition in the brains of very elderly adults. Neurology. 2013; 81(19): 1711-1718.

15. O'Rourke M. F., Safar M. E. Relationship between aortic stiffening and microvascular disease in brain and kidney: cause and logic of therapy. Hypertension. 2005; 46(1): 200-204.

16. Parker K. Are rapid changes in brain elasticity possible? Physics in Medicine and Biology. 2017; 62(18): 7425.

17. Boutouyrie P., Tropeano A. I., Asmar R., Gautier I., Benetos A., Lacolley P., Laurent S. Aortic stiffness is an independent predictor of primary coronary events in hypertensive patients: a longitudinal study. Hypertension. 2002; 39(1): 10-15.

18. Mattace-Raso F. U., van der Cammen T. J., Hofman A., van Popele N. M., Bos M. L., Schalekamp M., Asmar R., Reneman R. S., Hoeks A. P., Breteler M. M. Arterial stiffness and risk of coronary heart disease and stroke. Circulation. 2006; 113(5): 657-663.

19. Laurent S., Cockcroft J., Van Bortel L., Boutouyrie P., Giannattasio C., Hayoz D., Pannier B., Vlachopoulos C., Wilkinson I., Struijker-Boudier H. Expert consensus document on arterial stiffness: methodological issues and clinical applications. European Heart Journal. 2006; 27(21): 2588-2605.

20. Aki K., Richards P. G. Quantitative seismology. 2nd ed. Sausalito, Calif.: *University Science Books*; 2002. xviii, 700 p. p.

21. Tschoegl N. W. The phenomenological theory of linear viscoelastic behavior : an introduction. Berlin ; New York: *Springer-Verlag*; 1989. xxv, 769 p. p.

22. Carcione J. M. Wave fields in real media : wave propagation in anisotropic, anelastic, porous and electromagnetic media. 2nd ed. Amsterdam ; Boston: *Elsevier*; 2007. xxi, 515 p. p.

23. Hirsch S., Guo J., Reiter R., Papazoglou S., Kroencke T., Braun J., Sack I. MR elastography of the liver and the spleen using a piezoelectric driver, single-shot wave-field acquisition, and multifrequency dual parameter reconstruction. Magnetic Resonance in Medicine. 2014; 71(1): 267-277.

24. Papazoglou S., Hirsch S., Braun J., Sack I. Multifrequency inversion in magnetic resonance elastography. Physics in Medicine and Biology. 2012; 57(8): 2329-2346.

25. Tzschätzsch H., Guo J., Dittmann F., Hirsch S., Barnhill E., Jöhrens K., Braun J., Sack I. Tomoelastography by multifrequency wave number recovery from time-harmonic propagating shear waves. Medical Image Analysis. 2016; 30: 1-10.

26. Rump J., Klatt D., Braun J., Warmuth C., Sack I. Fractional encoding of harmonic motions in MR elastography. Magnetic Resonance in Medicine: An Official Journal of the International Society for Magnetic Resonance in Medicine. 2007; 57(2): 388-395.

27. Klein S., Staring M., Murphy K., Viergever M. A., Pluim J. P. elastix: a toolbox for intensity-based medical image registration. IEEE Transactions on Medical Imaging. 2010; 29(1): 196-205.

28. Bertalan G., Guo J., Tzschätzsch H., Klein C., Barnhill E., Sack I., Braun J. Fast tomoelastography of the mouse brain by multifrequency single-shot MR elastography. Magnetic Resonance in Medicine. 2019; 81(4): 2676-2687.

29. Hetzer S., Birr P., Fehlner A., Hirsch S., Dittmann F., Barnhill E., Braun J., Sack I. Perfusion alters stiffness of deep gray matter. Journal of Cerebral Blood Flow and Metabolism. 2018; 38(1): 116-125.

30. Cecelja M., Chowienczyk P. Role of arterial stiffness in cardiovascular disease. JRSM cardiovascular disease. 2012; 1(4): 1-10.

31. Fonck E., Feigl G. G., Fasel J., Sage D., Unser M., Rufenacht D. A., Stergiopulos N. Effect of aging on elastin functionality in human cerebral arteries. Stroke. 2009; 40(7): 2552-2556.

32. Hickson S. S., Butlin M., Graves M., Taviani V., Avolio A. P., McEniery C. M., Wilkinson I. B. The relationship of age with regional aortic stiffness and diameter. JACC: Cardiovascular Imaging. 2010; 3(12): 1247-1255.

33. Halloran B. G., Davis V. A., McManus B. M., Lynch T. G., Baxter B. T. Localization of aortic disease is associated with intrinsic differences in aortic structure. Journal of Surgical Research. 1995; 59(1): 17-22.

34. Kenyhercz W. E., Raterman B., Illapani V. S., Dowell J., Mo X., White R. D., Kolipaka A. Quantification of aortic stiffness using magnetic resonance elastography: Measurement reproducibility, pulse wave velocity comparison, changes over cardiac cycle, and relationship with age. Magnetic Resonance in Medicine. 2016; 75(5): 1920-1926.

35. Damughatla A. R., Raterman B., Sharkey-Toppen T., Jin N., Simonetti O. P., White R. D., Kolipaka A. Quantification of aortic stiffness using MR elastography and its comparison to MRI-based pulse wave velocity. Journal of Magnetic Resonance Imaging. 2015; 41(1): 44-51.

36. Redheuil A., Yu W. C., Wu C. O., Mousseaux E., de Cesare A., Yan R., Kachenoura N., Bluemke D., Lima J. A. Reduced ascending aortic strain and distensibility: earliest manifestations of vascular aging in humans. Hypertension. 2010; 55(2): 319-326.

37. Rogers W. J., Hu Y. L., Coast D., Vido D. A., Kramer C. M., Pyeritz R. E., Reichek N. Age-associated changes in regional aortic pulse wave velocity. Journal of the American College of Cardiology. 2001; 38(4): 1123-1129.

38. Klatt D., Papazoglou S., Braun J., Sack I. Viscoelasticity-based MR elastography of skeletal muscle. Physics in Medicine and Biology. 2010; 55(21): 6445.

39. Barnhill E., Kennedy P., Hammer S., van Beek E. J., Brown C., Roberts N. Statistical mapping of the effect of knee extension on thigh muscle viscoelastic properties using magnetic resonance elastography. Physiological Measurement. 2013; 34(12): 1675-1698.

40. Barth M., Breuer F., Koopmans P. J., Norris D. G., Poser B. A. Simultaneous multislice (SMS) imaging techniques. Magnetic Resonance in Medicine. 2016; 75(1): 63-81.

41. Schrank F., Warmuth C., Schaafs L. A., Tzschätzsch H., Elgeti T., Braun J., Sack I., Multi-frequency magnetic resonance elastography with spiral readout, respiratory navigator and stroboscopic wave sampling for cardiac stiffness mapping with high spatial and temporal resolution. ISMRM 27th Annual Meeting & Exhibition; 2019; Montreal, QC, Canada.

Appendix

A Synchronization
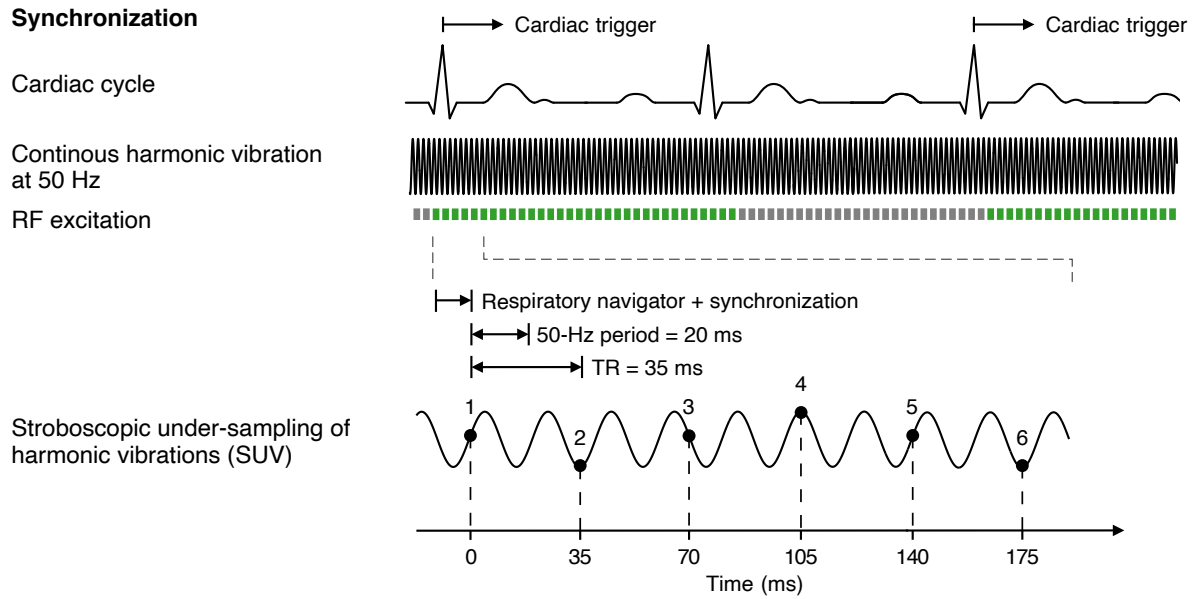
B Sequence diagram
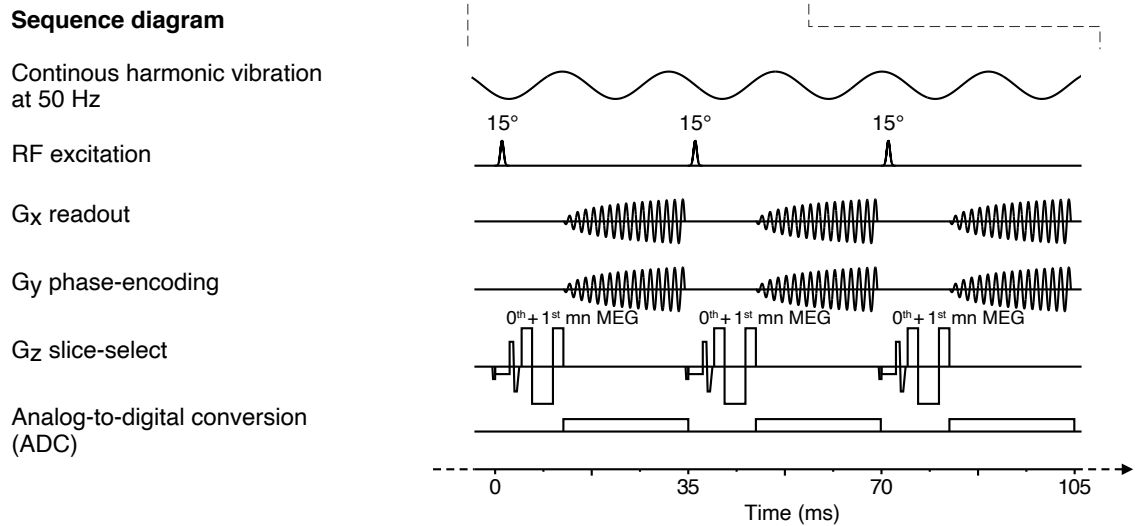
C Repetitions
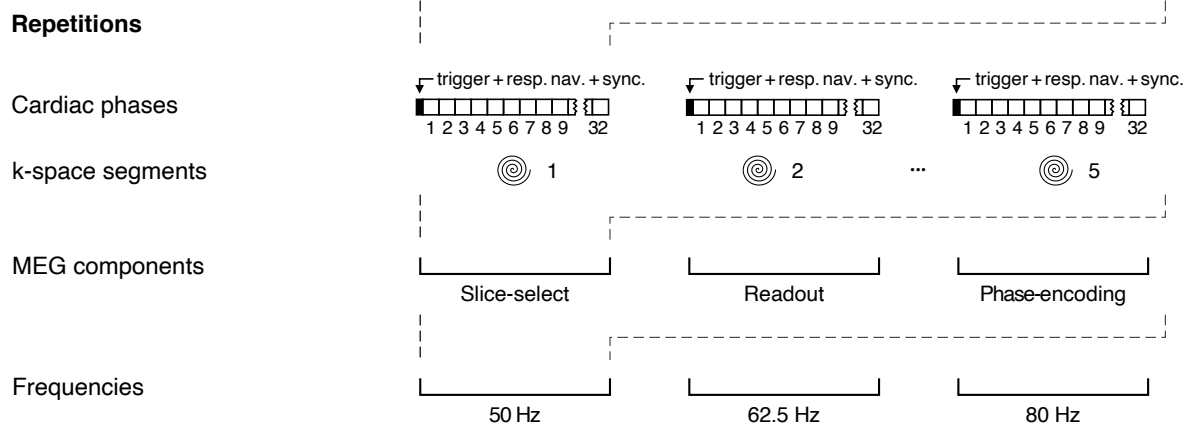
Figure A-1 Cardiac-gated ssMRE sequence used for the aorta examination in Study 2[11]. The main differences from the brain experiments are the respiratory navigation and adjusted pulse sequence parameter. **A** In addition to the delay time used to synchronize the vibration phase, a pencil beam navigator was used to compensate for the drifting movement of the aorta before the segmented image acquisition. Afterward, 32 images were acquired. The time of

repetition (TR) of 35 ms was intentionally mismatched to the vibration period of 20 ms to capture different wave dynamics successively due to their 15 ms time difference. **B** Gradient-echo spiral readout and low flip angle excitation allow for fast image acquisition and the sampling of multiple wave cycles within one cardiac cycle. **C** Cardiac triggering, vibration synchronization, respiratory navigation, and image acquisition are repeated for five k-space segments to complete the k-space, three orthogonal motion-encoding gradient (MEG) components, and three frequencies.

Statutory Declaration

"I, Felix Schrank, by personally signing this document in lieu of an oath, hereby affirm that I prepared the submitted dissertation on the topic *Time-resolved quantification of tissue structure by in vivo viscoelasticity measurements using magnetic resonance elastography / Zeitaufgelöste Charakterisierung von Gewebestrukturen mittels In-vivo-Bestimmung viskoelastischer Kenngrößen in der Magnetresonanz-Elastographie*, independently and without the support of third parties, and that I used no other sources and aids than those stated.

All parts which are based on the publications or presentations of other authors, either in letter or in spirit, are specified as such in accordance with the citing guidelines. The sections on methodology (in particular regarding practical work, laboratory regulations, statistical processing) and results (in particular regarding figures, charts and tables) are exclusively my responsibility.

Furthermore, I declare that I have correctly marked all of the data, the analyses, and the conclusions generated from data obtained in collaboration with other persons, and that I have correctly marked my own contribution and the contributions of other persons (cf. declaration of contribution). I have correctly marked all texts or parts of texts that were generated in collaboration with other persons.

My contributions to any publications to this dissertation correspond to those stated in the below joint declaration made together with the supervisor. All publications created within the scope of the dissertation comply with the guidelines of the ICMJE (International Committee of Medical Journal Editors; www.icmje.org) on authorship. In addition, I declare that I shall comply with the regulations of Charité – Universitätsmedizin Berlin on ensuring good scientific practice.

I declare that I have not yet submitted this dissertation in identical or similar form to another Faculty.

The significance of this statutory declaration and the consequences of a false statutory declaration under criminal law (Sections 156, 161 of the German Criminal Code) are known to me."

Date   Signature

Declaration of my own contribution to the publications

Felix Schrank contributed the following to the below listed publications:

Publication 1:

Schrank F., Warmuth C., Tzschätzsch H., Kreft B., Hirsch S., Braun J., Elgeti T., Sack I. Cardiac-gated steady-state multifrequency magnetic resonance elastography of the brain: Effect of cerebral arterial pulsation on brain viscoelasticity. Journal of Cerebral Blood Flow and Metabolism. 2020; 40(5): 991-1001. https://doi.org/10.1177/0271678X19850936

Contribution:

Prof. Ingolf Sack and I conceived the idea of investigating how cerebral arterial pulsation affects the brain's viscoelasticity and designed the experiments presented. This publication demonstrated the feasibility of the newly developed time-resolved steady-state MRE and introduced the method to the MRE community. Together with Prof. Ingolf Sack and Dr. Carsten Warmuth, I have developed the sequence and contributed significantly to the implementation of the steady-state MRE method. I validated the performance of the method with several phantom and volunteer experiments, tested the sequence timing and synchronization of the MRE hardware, and optimized pulse sequence parameters for brain imaging. Together with Dr. Heiko Tzschätzsch, I implemented the time-resolved post-processing pipeline and adjusted the inversion parameters. I individually organized and conducted each experiment, including the recruitment of participants, the operation of the MRI unit, and the blood pressure measurements. I performed the complete data analysis and statistical evaluation, including post-processing, SNR analysis, correlation analysis, and hypothesis testing using R and MATLAB. Together with Prof. Ingolf Sack, I wrote and edited the manuscript. All findings presented in the publication result from my data analysis and statistical tests. Each figure and table presented (Figures 1–6, Table 1) was created by me and is based on my analysis. All co-authors provided valuable feedback on the experiments and interpreted the results, developed the pneumatic MRE actuators used, and revised the manuscript.

Publication 2:

Schaafs L. A.*, **Schrank F.***, Warmuth C., Steffen I. G., Braun J., Hamm B., Sack I., Elgeti T. Steady-State Multifrequency Magnetic Resonance Elastography of the Thoracic and Abdominal Human Aorta–Validation and Reference Values. Investigative Radiology. 2020; 55(7): 451-456. https://doi.org/10.1097/RLI.0000000000000654
*Lars-Arne Schaafs and Felix Schrank contributed equally to this work.

Contribution:

Dr. Thomas Elgeti, Dr. Lars-Arne Schaafs, and I developed the idea to use the new fast steady-state MRE method presented in publication 1 to quantify the viscoelasticity of the thoracic aorta for the first time. Together with Dr. Lars-Arne Schaafs, I designed and organized the experiments. I was individually

responsible for validating the feasibility with several phantoms and experiments on volunteers. I optimized the pulse sequence parameters for aortic imaging and the MRE hardware configuration with appropriate frequencies. Dr. Lars-Arne Schaafs and I conducted all experiments. All of the presented data analysis is based on my data post-processing. Together with Dr. Lars-Arne Schaafs, I contributed significantly to data analysis, performance evaluation, and statistical testing. Dr. Thomas Elgeti, Dr. Lars-Arne Schaafs, and I wrote and edited the manuscript. All findings presented in the publication result from my post-processing and MRE-parameter reconstruction. Figures 2 and S2 were prepared by me and were the result of my SNR analysis and post-processing. Figures 4 and 5 were the result of my reconstructed stiffness maps. All co-authors contributed to the analysis and statistics, provided valuable feedback on the interpretation of the data, and reviewed the manuscript.

Publication 3:

Schrank F., Warmuth C., Görner S., Meyer T., Tzschätzsch H., Guo J., Uca Y. O., Elgeti T., Braun J., Sack I. Real-time MR elastography for viscoelasticity quantification in skeletal muscle during dynamic exercises. Magnetic Resonance in Medicine. 2020; 84(1): 103-114. https://doi.org/10.1002/mrm.28095

Contribution:

Prof. Ingolf Sack and I developed the idea of real-time MRE as an extension of the steady-state MRE method published in publications 1 and 2. Together with Prof. Ingolf Sack and Steffen Görner, I developed the hypotheses and designed the experiments on the lower leg muscles. I significantly contributed to the development and implementation of real-time MRE. I tested the pulse sequence timing, performed preliminary phantom and volunteer studies, and adjusted the post-processing pipeline to account for the interlaced image acquisition of real-time MRE. I organized and conducted all experiments myself, including the recruitment of participants and the operation of the MRI unit. All data analysis and statistical tests were individually performed by me, including post-processing, SNR analysis, ROI selection, and hypothesis testing of mixed-effects models. Based on my results and statistical significance, Prof. Ingolf Sack and I wrote and edited the manuscript. All illustrations, except Figure 7, were created by me and based on my analyses and findings. Table 1 is the result of my statistical analysis. All co-authors provided valuable feedback on the experiments and the manuscript.

_____

Signature, date and stamp of first supervising university professor / lecturer

_____

Signature of doctoral candidate

Publication 1: Cardiac-gated steady-state multifrequency magnetic resonance elastography of the brain: Effect of cerebral arterial pulsation on brain viscoelasticity

Journal Data Filtered By: **Selected JCR Year: 2017** Selected Editions: SCIE,SSCI
Selected Categories: **"HEMATOLOGY"** Selected Category Scheme: WoS
Gesamtanzahl: 71 Journale

Rank	Full Journal Title	Total Cites	Journal Impact Factor	Eigenfactor Score
1	CIRCULATION RESEARCH	52,753	15.211	0.082820
2	BLOOD	167,858	15.132	0.278040
3	Lancet Haematology	1,307	10.698	0.007350
4	LEUKEMIA	25,265	10.023	0.059580
5	HAEMATOLOGICA	16,138	9.090	0.038930
6	Journal of Hematology & Oncology	4,098	7.333	0.009750
7	BLOOD REVIEWS	2,810	6.600	0.006010
8	ARTERIOSCLEROSIS THROMBOSIS AND VASCULAR BIOLOGY	34,074	6.086	0.044820
9	JOURNAL OF CEREBRAL BLOOD FLOW AND METABOLISM	19,450	6.045	0.028280
10	STEM CELLS	21,694	5.587	0.035680
11	AMERICAN JOURNAL OF HEMATOLOGY	9,458	5.303	0.022620
12	BRITISH JOURNAL OF HAEMATOLOGY	23,861	5.128	0.039010
13	THROMBOSIS AND HAEMOSTASIS	16,701	4.952	0.025770
14	JOURNAL OF THROMBOSIS AND HAEMOSTASIS	17,663	4.899	0.034380
15	BONE MARROW TRANSPLANTATION	12,506	4.497	0.020810
16	CRITICAL REVIEWS IN ONCOLOGY HEMATOLOGY	6,956	4.495	0.012190
17	BIOLOGY OF BLOOD AND MARROW TRANSPLANTATION	10,583	4.484	0.026940
18	JOURNAL OF LEUKOCYTE BIOLOGY	17,244	4.224	0.021200
19	TRANSFUSION MEDICINE REVIEWS	1,292	4.111	0.002350
20	CYTOTHERAPY	5,589	3.993	0.009020
21	SEMINARS IN HEMATOLOGY	2,305	3.926	0.003780
22	TRANSFUSION	13,045	3.423	0.022050
23	SEMINARS IN THROMBOSIS AND HEMOSTASIS	3,876	3.345	0.006270
24	STEM CELLS AND DEVELOPMENT	7,589	3.315	0.016440

Schrank F., Warmuth C., Tzschätzsch H., Kreft B., Hirsch S., Braun J., Elgeti T., Sack I. Cardiac-gated steady-state multifrequency magnetic resonance elastography of the brain: Effect of cerebral arterial pulsation on brain viscoelasticity. Journal of Cerebral Blood Flow and Metabolism. 2020; 40(5): 991-1001. https://doi.org/10.1177/0271678X19850936

Publication 2: Steady-state multifrequency magnetic resonance elastography of the thoracic and abdominal human aorta—validation and reference values

Schaafs L. A.*, **Schrank F.***, Warmuth C., Steffen I. G., Braun J., Hamm B., Sack I., Elgeti T. Steady-State Multifrequency Magnetic Resonance Elastography of the Thoracic and Abdominal Human Aorta–Validation and Reference Values. Investigative Radiology. 2020; 55(7): 451-456.

https://doi.org/10.1097/RLI.0000000000000654

*Lars-Arne Schaafs and Felix Schrank contributed equally to this work.

Journal Data Filtered By: **Selected JCR Year: 2018** Selected Editions: SCIE,SSCI
Selected Categories: **"RADIOLOGY, NUCLEAR MEDICINE and MEDICAL IMAGING"** Selected Category Scheme: WoS
Gesamtanzahl: 129 Journale

Rank	Full Journal Title	Total Cites	Journal Impact Factor	Eigenfactor Score
1	JACC-Cardiovascular Imaging	8,801	10.975	0.026160
2	MEDICAL IMAGE ANALYSIS	7,694	8.880	0.013370
3	IEEE TRANSACTIONS ON MEDICAL IMAGING	19,545	7.816	0.024990
4	RADIOLOGY	54,641	7.608	0.061300
5	JOURNAL OF NUCLEAR MEDICINE	27,551	7.354	0.037990
6	EUROPEAN JOURNAL OF NUCLEAR MEDICINE AND MOLECULAR IMAGING	15,406	7.182	0.024760
7	CLINICAL NUCLEAR MEDICINE	4,922	6.498	0.007680
8	INTERNATIONAL JOURNAL OF RADIATION ONCOLOGY BIOLOGY PHYSICS	45,833	6.203	0.046810
9	INVESTIGATIVE RADIOLOGY	6,563	6.091	0.011150
10	Circulation-Cardiovascular Imaging	5,456	5.813	0.018480
11	NEUROIMAGE	99,720	5.812	0.132720
12	ULTRASOUND IN OBSTETRICS & GYNECOLOGY	12,336	5.595	0.020140
13	European Heart Journal-Cardiovascular Imaging	5,498	5.260	0.021650
14	RADIOTHERAPY AND ONCOLOGY	17,873	5.252	0.027470
15	Photoacoustics	512	5.250	0.001330
16	JOURNAL OF CARDIOVASCULAR MAGNETIC RESONANCE	5,113	5.070	0.014020
17	ULTRASCHALL IN DER MEDIZIN	2,238	4.613	0.003700
18	HUMAN BRAIN MAPPING	22,040	4.554	0.043230
19	JOURNAL OF NUCLEAR CARDIOLOGY	3,711	4.112	0.004480
20	EUROPEAN RADIOLOGY	19,597	3.962	0.033870

Schaafs L. A.*, Schrank F.*, Warmuth C., Steffen I. G., Braun J., Hamm B., Sack I., Elgeti T. Steady-State Multifrequency Magnetic Resonance Elastography of the Thoracic and Abdominal Human Aorta–Validation and Reference Values. Investigative Radiology. 2020; 55(7): 451-456. https://doi.org/10.1097/RLI.0000000000000654

*Lars-Arne Schaafs and Felix Schrank contributed equally to this work.

Publication 3: Real-time MR elastography for viscoelasticity quantification in skeletal muscle during dynamic exercises

Schrank F., Warmuth C., Görner S., Meyer T., Tzschätzsch H., Guo J., Uca Y. O., Elgeti T., Braun J., Sack I. Real-time MR elastography for viscoelasticity quantification in skeletal muscle during dynamic exercises. Magnetic Resonance in Medicine. 2020; 84(1): 103-114. https://doi.org/10.1002/mrm.28095

Journal Data Filtered By: **Selected JCR Year: 2018** Selected Editions: SCIE,SSCI
Selected Categories: **"RADIOLOGY, NUCLEAR MEDICINE and MEDICAL IMAGING"** Selected Category Scheme: WoS
Gesamtanzahl: 129 Journale

Rank	Full Journal Title	Total Cites	Journal Impact Factor	Eigenfactor Score
1	JACC-Cardiovascular Imaging	8,801	10.975	0.026160
2	MEDICAL IMAGE ANALYSIS	7,694	8.880	0.013370
3	IEEE TRANSACTIONS ON MEDICAL IMAGING	19,545	7.816	0.024990
4	RADIOLOGY	54,641	7.608	0.061300
5	JOURNAL OF NUCLEAR MEDICINE	27,551	7.354	0.037990
6	EUROPEAN JOURNAL OF NUCLEAR MEDICINE AND MOLECULAR IMAGING	15,406	7.182	0.024760
7	CLINICAL NUCLEAR MEDICINE	4,922	6.498	0.007680
8	INTERNATIONAL JOURNAL OF RADIATION ONCOLOGY BIOLOGY PHYSICS	45,833	6.203	0.046810
9	INVESTIGATIVE RADIOLOGY	6,563	6.091	0.011150
10	Circulation-Cardiovascular Imaging	5,456	5.813	0.018480
11	NEUROIMAGE	99,720	5.812	0.132720
12	ULTRASOUND IN OBSTETRICS & GYNECOLOGY	12,336	5.595	0.020140
13	European Heart Journal-Cardiovascular Imaging	5,498	5.260	0.021650
14	RADIOTHERAPY AND ONCOLOGY	17,873	5.252	0.027470
15	Photoacoustics	512	5.250	0.001330
16	JOURNAL OF CARDIOVASCULAR MAGNETIC RESONANCE	5,113	5.070	0.014020
17	ULTRASCHALL IN DER MEDIZIN	2,238	4.613	0.003700
18	HUMAN BRAIN MAPPING	22,040	4.554	0.043230
19	JOURNAL OF NUCLEAR CARDIOLOGY	3,711	4.112	0.004480
20	EUROPEAN RADIOLOGY	19,597	3.962	0.033870

Rank	Full Journal Title	Total Cites	Journal Impact Factor	Eigenfactor Score
21	RADIOGRAPHICS	11,768	3.923	0.009170
22	Biomedical Optics Express	9,547	3.910	0.021750
23	MAGNETIC RESONANCE IN MEDICINE	32,648	3.858	0.034990
24	SEMINARS IN NUCLEAR MEDICINE	2,245	3.798	0.002710
25	Journal of the American College of Radiology	4,191	3.785	0.009760
26	JOURNAL OF MAGNETIC RESONANCE IMAGING	17,147	3.732	0.027800
27	KOREAN JOURNAL OF RADIOLOGY	2,687	3.730	0.004800
28	INTERNATIONAL JOURNAL OF HYPERTHERMIA	3,552	3.589	0.004020
29	EJNMMI Physics	394	3.475	0.001350
30	NMR IN BIOMEDICINE	7,511	3.414	0.014790
31	MOLECULAR IMAGING AND BIOLOGY	2,543	3.341	0.005360
32	Journal of Cardiovascular Computed Tomography	1,711	3.316	0.004430
33	COMPUTERIZED MEDICAL IMAGING AND GRAPHICS	2,464	3.298	0.002990
34	AMERICAN JOURNAL OF NEURORADIOLOGY	23,231	3.256	0.028010
35	MEDICAL PHYSICS	26,715	3.177	0.030870
36	AMERICAN JOURNAL OF ROENTGENOLOGY	33,633	3.161	0.028540
37	CANCER IMAGING	1,406	3.153	0.002220
38	Quantitative Imaging in Medicine and Surgery	1,072	3.074	0.002420
39	PHYSICS IN MEDICINE AND BIOLOGY	27,458	3.030	0.031970
40	EJNMMI Research	1,408	3.000	0.004320
41	EUROPEAN JOURNAL OF RADIOLOGY	12,871	2.948	0.019480
42	Radiation Oncology	5,669	2.895	0.012980

Selected JCR Year: 2018; Selected Categories: "RADIOLOGY, NUCLEAR MEDICINE and MEDICAL IMAGING"

Schrank F., Warmuth C., Görner S., Meyer T., Tzschätzsch H., Guo J., Uca Y. O., Elgeti T., Braun J., Sack I. Real-time MR elastography for viscoelasticity quantification in skeletal muscle during dynamic exercises. Magnetic Resonance in Medicine. 2020; 84(1): 103-114. https://doi.org/10.1002/mrm.28095

My curriculum vitae does not appear in the electronic version of my paper for reasons of data protection.

My curriculum vitae does not appear in the electronic version of my paper for reasons of data protection.

My curriculum vitae does not appear in the electronic version of my paper for reasons of data protection.

List of publications

Original publications

Schaafs L. A.*, **Schrank F.***, Warmuth C., Steffen I. G., Braun J., Hamm B., Sack I., Elgeti T. Steady-State Multifrequency Magnetic Resonance Elastography of the Thoracic and Abdominal Human Aorta–Validation and Reference Values. Investigative Radiology. 2020; 55(7): 451-456.

https://doi.org/10.1097/RLI.0000000000000654

*Lars-Arne Schaafs and Felix Schrank contributed equally to this work.

Journal impact factor: 6.091 (JCR 2018)

Mura J., **Schrank F.***, Sack I. An analytical solution to the dispersion-by-inversion problem in magnetic resonance elastography. Magnetic Resonance in Medicine. 2020; 84(1): 61-71.

https://doi.org/10.1002/mrm.28247

*Joaquin Mura and Felix Schrank contributed equally to this work.

Journal impact factor: 3.858 (JCR 2018)

Kreft B., Tzschätzsch H., **Schrank F.**, Bergs J., Streitberger K. J., Wäldchen S., Hetzer S., Braun J., Sack I. Time-Resolved Response of Cerebral Stiffness to Hypercapnia in Humans. Ultrasound in Medicine and Biology. 2020; 46(4): 936-943.

https://doi.org/10.1016/j.ultrasmedbio.2019.12.019

Journal impact factor: 2.205 (JCR 2018)

Streitberger K. J., Lilaj L., **Schrank F.**, Braun J., Hoffmann K. T., Reiss-Zimmermann M., Käs J. A., Sack I. How tissue fluidity influences brain tumor progression. Proceedings of the National Academy of Sciences of the United States of America. 2020; 117(1): 128-134.

https://doi.org/10.1073/pnas.1913511116

Journal impact factor: 9.580 (JCR 2018)

Schrank F., Warmuth C., Görner S., Meyer T., Tzschätzsch H., Guo J., Uca Y. O., Elgeti T., Braun J., Sack I. Real-time MR elastography for viscoelasticity quantification in skeletal muscle during dynamic exercises. Magnetic Resonance in Medicine. 2020; 84(1): 103-114.

https://doi.org/10.1002/mrm.28095

Journal impact factor: 3.858 (JCR 2018)

Schrank F., Warmuth C., Tzschätzsch H., Kreft B., Hirsch S., Braun J., Elgeti T., Sack I. Cardiac-gated steady-state multifrequency magnetic resonance elastography of the brain: Effect of cerebral arterial pulsation on brain viscoelasticity. Journal of Cerebral Blood Flow and Metabolism. 2020; 40(5): 991-1001.

https://doi.org/10.1177/0271678X19850936

Journal impact factor: 6.045 (JCR 2017)

de Schellenberger A. A., Tzschätzsch H., Polchlopek B., Bertalan G., **Schrank F.**, Garczynska K., Janmey P. A., Braun J., Sack I. Sensitivity of multifrequency magnetic resonance elastography and diffusion-weighted imaging to cellular and stromal integrity of liver tissue. Journal of Biomechanics. 2019; 88: 201-208.

https://doi.org/10.1016/j.jbiomech.2019.03.037

Journal impact factor: 2.431 (2017)

Sauer F., Oswald L., Ariza de Schellenberger A., Tzschätzsch H., **Schrank F.**, Fischer T., Braun J., Mierke C. T., Valiullin R., Sack I., Käs J. A. Collagen networks determine viscoelastic properties of connective tissues yet do not hinder diffusion of the aqueous solvent. Soft Matter. 2019; 15(14): 3055-3064.

https://doi.org/10.1039/C8SM02264J

Journal impact factor: 3.709 (JCR 2017)

Tzschätzsch H., Kreft B., **Schrank F.**, Bergs J., Braun J., Sack I. In vivo time-harmonic ultrasound elastography of the human brain detects acute cerebral stiffness changes induced by intracranial pressure variations. Scientific Reports. 2018; 8(1): 17888.

https://doi.org/10.1038/s41598-018-36191-9

Journal impact factor: 4.122 (JCR 2017)

Patents

Sack I., Braun J., Tzschätzsch H., Warmuth C., **Schrank F.**, Guo J., Schultz M. Real-time MR elastography, DE 2019022514243800 (World patent application pending)

Acknowledgements

First of all, I would like to thank Prof. Ingolf Sack, head of the MRE research group at Charité - Universitätsmedizin Berlin, to supervise and monitor my doctoral studies. He has given me invaluable feedback, critical suggestions, and enormous motivation over the past three years. Without his support, patience, and trust, my professional success and personal development would not have been possible. Thank you very much. It was a sheer delight to work with you.

I am grateful to Prof. Jeanette Schulz-Menger for investing her time and giving helpful and critical advice from a clinical perspective. I am genuinely thankful to the entire MRE research group for their continuous support, the inspiring discussions, and the exciting community projects that made the daily work so enjoyable. I would especially like to thank Dr. Carsten Warmuth. His knowledge, continuous support, and commitment have made this thesis possible. I would also like to thank Dr. Jürgen Braun for his full support and invaluable advice. In addition to the persons mentioned above, I would like to thank Anna-Sophie Morr, Bernhard Kreft, Gergely Bertalan, Heiko Tzschätzsch, Helge Herthum, Jing Guo, Joachim Snellings, Judith Bergs, Karolina Garczynska, Ledia Lilaj, Mehrgan Shahryari, Jürgen Braun, Steffen Görner, Tom Meyer, Yang Yang, Stephan Marticorena Garcia, Eric Barnhill, Stefan Hetzer, Sebastian Hirsch, Lars-Arne Schaafs, and Thomas Elgeti.

Lastly, my family and friends deserve endless gratitude. Many thanks, Silke, Peter, and Leonard, for your motivation, encouragement, and unlimited support. Cindy, Lucia, and Ella, I am deeply grateful for your support, love, and trust. Thank you so much for the fantastic and unforgettable three years.